



Contents lists available at ScienceDirect

Remote Sensing of Environment

journal homepage: www.elsevier.com/locate/rse

Atmospheric correction over coastal waters with aerosol properties constrained by multi-pixel observations

Junwei Wang^a, Zhongping Lee^{b,*}, Daosheng Wang^a, Shaoling Shang^a, Jianwei Wei^{b,c}, Alex Gilerson^d

^a State Key Laboratory of Marine Environmental Science, College of Ocean and Earth Sciences, Xiamen University, Xiamen 361102, China

^b School for the Environment, University of Massachusetts Boston, Boston, MA 02125, USA

^c NOAA Center for Satellite Applications and Research, 5830 University Research Ct., College Park, MD 20740, USA

^d Optical Remote Sensing Laboratory, The City College of the City University of New York, New York, NY, 10031, USA

ARTICLE INFO

Edited by: Dr. Menghua Wang.

Keywords:

Ocean color remote sensing
Atmospheric correction
Multi-pixel observations
Landsat-8 OLI

ABSTRACT

We propose an innovative multi-pixel atmospheric correction approach (MPACA) to process high-spatial-resolution satellite measurements over coastal waters based on a revised POLYMER model. MPACA assumes the aerosol type to be uniform within a relatively small region, while the aerosol load and water properties are allowed to vary. Landsat-8 OLI images over six coastal locations with various turbidities were utilized to evaluate the performance of MPACA. The retrieved remote sensing reflectance ($R_{rs}(\lambda)$) by MPACA is validated with *in situ* matchups obtained from two sources: ship-based field campaigns and the AERONET-OC networks. It is found that, at each of OLI's four visible bands, MPACA provided accurate $R_{rs}(\lambda)$ products over such coastal environments, with the Root Mean Square Difference (RMSD) and Mean Absolute Percentage Difference (MAPD) less than 0.0006 sr^{-1} and 16.2%, respectively. In contrast, the $R_{rs}(\lambda)$ values retrieved with NASA's SeaDAS (v7.5), where each pixel was treated independently, showed RMSD and MAPD as $\sim 0.0018 \text{ sr}^{-1}$ and $\sim 38.8\%$, respectively. Acolite-DSF, which assumed some spatial dependency, obtained MAPD almost two times that of SeaDAS for each visible band. Further, it appears that Acolite-EXP did not perform well for this evaluation dataset, where RMSD is $\sim 0.0062 \text{ sr}^{-1}$ and MAPD is $\sim 228.2\%$. These results suggest that MPACA is a promising scheme for atmospheric correction in coastal waters, especially for measurements from multi-band satellites that have a high spatial resolution along with at least two bands in the NIR or SWIR domain.

1. Introduction

In recent years, high-spatial-resolution (HSR) sensors, airborne and spaceborne, have been frequently used to observe coastal and inland aquatic environments. These sensors include NASA Earth Observing-1 (EO-1) Hyperion satellite launched in 2000 (Brando and Dekker, 2003; Lee et al., 2007; Zhu and Yu, 2012), WorldView series in mid-2000 (Doxani et al., 2012; Lee et al., 2012; Reshitnyk et al., 2014), the Operational Land Imager (OLI) onboard the latest Landsat-8 in 2013 (De Keukelaere et al., 2018; Franz et al., 2015a; Pacheco et al., 2015; Vanhellemont and Ruddick, 2015), and the Multi-spectral Instrument (MSI) onboard Sentinel-2 (S2) in 2015 and 2017, respectively (Pahlevan et al., 2017b; Toming et al., 2016). Measurements from these sensors, with high spatial resolution, have greatly improved the observations of biogeochemical properties in coastal waters and inland lakes, where the

occurrence of red tides or harmful algae blooms is becoming more frequent in recent decades (Lim and Choi, 2015; Cracknell et al., 2001; Doxani et al., 2012; Pahlevan et al., 2019; Toming et al., 2016).

For satellite measurements over aquatic environments, the total radiance at the top-of-atmosphere (L_t) is the sum of the radiance from the atmosphere (L_{path}), sea surface reflectance, and that coming out of a water body, with the last commonly termed as water-leaving radiance (L_w). L_w contains information through the scattering and absorption processes induced by various constituents within water, but it only makes about $\sim 20\%$ of L_t over turbid coastal waters (IOCCG, 2010). Therefore, an essential step in the ocean (water) color remote sensing is to retrieve L_w from L_t as accurately as possible, a procedure referred to as atmospheric correction (AC), and many AC algorithms have been proposed since the 1970s. Commonly, the overall scheme of ACs is to adequately estimate the signal of each non-water component

* Corresponding author.

E-mail address: ZhongPing.Lee@umb.edu (Z. Lee).

<https://doi.org/10.1016/j.rse.2021.112633>

Received 9 October 2020; Received in revised form 26 July 2021; Accepted 31 July 2021

0034-4257/© 2021 Elsevier Inc. All rights reserved.

contributing to L_t . Among them, the most critical step is to evaluate both aerosol density (indicated by the aerosol optical depth at a reference wavelength-AOD(λ_0)) and type (indicated by the single scattering albedo ω_0) for each pixel independently. After performing Rayleigh correction (Gordon and Wang, 1992; Wang, 2002, 2005) on L_t , AOD(λ_0) and ω_0 are determined using information in the near-infrared (NIR) band, where pre-developed look-up tables (LUTs) (Ahmad et al., 2010; Gordon and Wang, 1994) and a “black pixel” assumption in the NIR bands (for oceanic and most coastal waters) are implemented (Ahn et al., 2012; Gordon, 1997; Gordon and Wang, 1994). The atmospheric contributions in the visible bands are further estimated; subsequently, L_w in this spectral domain is calculated by subtracting off the atmospheric contributions from L_t . As highlighted in the report (IOCCG, 2010) distributed by the International Ocean Color Coordinating Group (IOCCG), the above AC schemes can derive accurate aquatic reflectance over the open ocean, but still contain large uncertainties in turbid coastal and inland waters due to strong particle backscattering in the NIR bands (IOCCG, 2010; Pahlevan et al., 2020). For non-zero NIR water reflectance in turbid coastal waters, Bailey et al. (2010) used an iterative approach based on the retrieved chlorophyll-a concentration (Chl-a) to estimate L_w (NIR). But it is found that such an approach is not applicable in turbid waters (Dogliotti et al., 2016). Moore et al. (1999) developed a bright-pixel atmospheric correction algorithm (BPAC) for MERIS data over turbid waters. They estimated the contributions of sediments to R_{rs} (NIR) iteratively, with relationships between the inherent optical properties (IOPs) and suspended particulate matter (SPM) developed for the Humber estuary, UK. Some researchers have found that BPAC gave negative reflectance in the blue bands due to an overestimation of R_{rs} (NIR), which suggested that the IOP models of BPAC might not be suitable for other coastal waters (Bi et al., 2018; Lavender et al., 2005; Majazi et al., 2014).

In view of the issues associated with NIR bands, researchers have extended the “black pixel” assumption to SWIR bands (Vanhellemont and Ruddick, 2015; Wang and Shi, 2007). However, a lack of SWIR bands (e.g., MEdium Resolution Imaging Spectrometer-MERIS, Sea-Viewing Wide Field-of-View Sensor-SeaWiFS, and some sensors on small satellites) or low signal-to-noise ratio (SNR) in the SWIR bands (e.g., Landsat-8 OLI) (Cao et al., 2018b; Li et al., 2017) has limited the utilization of this strategy for accurately characterizing aerosol properties.

Separately, there are also several practices of atmospheric correction based on machine learning to process satellite measurements over complex atmospheric-coastal environments (Brajard et al., 2008; Doerffer and Schiller, 2007; Fan et al., 2017; Fan et al., 2020). For example, recently, Fan et al. (2017, 2020) developed a new system, Ocean Color – Simultaneous Marine and Aerosol Retrieval Tool (OC-SMART), to derive bio-optical parameters from L_t obtained by ocean color satellites (e.g., SeaWiFS, Visible Infrared Imaging Radiometer-VIIRS, Landsat-8, etc.). OC-SMART, as a data analysis platform, applied multilayer neural networks to directly estimate R_{rs} and AOD from Rayleigh-corrected radiance (L_{rc}) in the visible-NIR spectral domain, and it was indicated that OC-SMART is applicable from clear waters to highly turbid waters (Fan et al., 2017; Fan et al., 2020). However, the application of such empirical schemes requires the targeted area at the time of observation to have similar atmospheric and oceanic characteristics as those covered by the training data, an unknown prerequisite.

In the above AC systems, a key aspect is to treat each pixel within an image independently; therefore, the spatial relationship of aerosol properties among neighboring pixels is ignored. Hu et al. (2000) demonstrated that the spatial variation of atmospheric properties (in particular the aerosol types) is far weaker than that of water properties. Thus the aerosol properties over clear waters could be applied to nearby turbid waters for the derivation of L_w for the latter. We may extend this principle to HSR data, as the swath of an HSR image is usually 10's-100's km or narrower, and the spatial resolution ranges from submeter to 10's of meters, so that the pixel-to-pixel variation of atmospheric properties

is even less compared to that presented in Hu et al. (2000). Further, computing technology has significantly advanced in recent decades, where processing multiple pixels simultaneously within an ocean color image is no longer an insurmountable computational burden. In this paper, we thus present an innovative AC scheme (Multi-Pixel Atmospheric Correction Algorithm, MPACA) to process HSR image data, where the atmospheric properties of each pixel within a scene are constrained using measurements from multiple pixels, while the water properties of each pixel remain varying independently. As a demonstration, MPACA was applied to Landsat-8 OLI measurements of six coastal locations with different turbidities. We evaluated the algorithm performance through comparison with *in situ* measurements. We also compared the performance with other conventional AC approaches adopted in SeaDAS (Bailey et al., 2010) and the Acolite modules (Vanhellemont and Ruddick, 2015, 2018).

2. Atmospheric correction approaches

2.1. Brief summary of a few existing atmospheric correction approaches for OLI data

The total reflectance at top-of-atmosphere (ρ_t) over water, defined as $\pi L_t / (\cos(\theta_s) F_0)$, can be expressed as (Gordon and Wang, 1994; Steinmetz et al., 2011):

$$\rho_t(\lambda) = t_g(\lambda) [\rho_r(\lambda) + \rho_a(\lambda) + \rho_{ra}(\lambda) + t_s(\lambda)T(\lambda)\rho_{sg} + t_s(\lambda)t_v(\lambda)\pi R_{rs}(\lambda)] \quad (1)$$

Here F_0 is the extraterrestrial solar irradiance (Thuillier et al., 1998), t_g the gas transmittance, ρ_r the Rayleigh reflectance, ρ_a the aerosol reflectance, ρ_{ra} the molecule-aerosol coupled reflectance, ρ_{sg} the sun glint reflectance, T the direct transmittance, and R_{rs} the remote-sensing reflectance of the water body (including bottom contributions of optically shallow waters). t_s and t_v are the diffuse atmospheric transmittance at the solar zenith angle (θ_s) and sensor viewing angle (θ_v), respectively. As it is R_{rs} that contains information of constituents in water, the ultimate goal of an AC algorithm is to obtain R_{rs} (or normalized water-leaving radiance L_{wm}) as accurately as possible. IOCCG Report #10 (2010) has detailed descriptions of various AC algorithms developed in the past decades. A few revisions or variations are adapted for processing Landsat-8 OLI measurements, which are briefly described below.

2.1.1. NASA standard approach

The NASA standard approach is part of the SeaDAS data processing system (v7.5) (Franz et al., 2015b). Specifically, the transmittance of the gaseous layer is expressed as a product of the optical depth of the atmospheric gas (e.g., the ozone- O_3 , nitrogen dioxide- NO_2 (Ahmad et al., 2007), or water vapor- H_2O (Chou, 1981), etc.). Rayleigh and aerosol reflectance are stored in LUTs in advance (Ahmad et al., 2010; Wang, 2002, 2005). The contribution of sun glint is determined by environmental conditions (Wang and Bailey, 2001). As described above, the estimation of aerosol reflectance is based on Gordon and Wang (1994) approach, which uses a pair of bands in the NIR or SWIR bands. For Landsat-8 OLI image over coastal waters, the choice of band combination is one NIR band (865 nm) and one SWIR band (1609 nm) (Franz et al., 2015a; Pahlevan et al., 2017b), which takes advantage of the strong water absorption at the SWIR wavelength (Vanhellemont and Ruddick, 2015; Wang and Shi, 2007). Meanwhile, to loosen up the restriction of the “black pixel” assumption, an iterative bio-optical modeling scheme is utilized to estimate R_{rs} at the NIR band (Bailey et al., 2010), then the aerosol reflectance at the NIR band is estimated after removing R_{rs} (NIR). This algorithm requires the relationships between R_{rs} (NIR) and Chl-a to be valid and high accuracy in estimating Chl-a.

2.1.2. Acolite-EXP approach

Acolite is a publicly available AC processing package, which is

specifically developed for processing high-spatial-resolution measurements (e.g., Landsat-8 OLI and Sentinel-2 MSI) (Vanhellemont and Ruddick, 2014). The EXP scheme uses two SWIR-bands based exponential extrapolation (EXP) method (v20210114.0) to determine aerosol reflectance (Vanhellemont and Ruddick, 2015), with R_{rs} considered negligible at the two SWIR bands (1609 nm and 2202 nm). Then the aerosol reflectance at the visible spectral domain is extrapolated by an exponential spectrum from the two SWIR wavelengths. Due to low signal and low SNR at these two SWIR bands for Landsat-8 OLI, it may produce noisy R_{rs} outputs for various pixels (Pahlevan et al., 2017a; Werdell et al., 2010).

2.1.3. Acolite-DSF approach

The dark spectrum fitting (DSF) scheme (Vanhellemont, 2020; Vanhellemont and Ruddick, 2018) of Acolite (v20210114.0) is an image-based approach, which estimates the atmospheric path reflectance (ρ_{path}) within a targeted (sub)scene based on two assumptions. First, it is assumed that ρ_{path} remains the same spatially in a certain study area; second, the study area contains pixels with R_{rs} being zero at least for one of the bands, where ρ_{path} can be estimated. Based on these two assumptions, the atmospheric path reflectance is estimated from multiple dark targets in the (sub)scene. These dark targets are selected accordingly to the lowest values of ρ_t after the correction of gas and air-water interface reflectance (Gordon et al., 1988) in all bands.

To account for the potential spatial variability of atmospheric properties over a large area, an OLI image is divided into several tiles with a size of about 6 km × 6 km. For each separate tile, based on the assumption of ρ_{path} being constant, the water reflectance of each tile can be estimated by removing a spatially uniform ρ_{path} . Finally, the parameters of the entire image are composed of the retrieved parameters from different tiles, where linear interpolation is employed to smooth adjacent tiles.

The above-mentioned AC algorithms for processing Landsat-8 OLI images, except Acolite-DSF, are all based on the strategy of treating each pixel in an image independently. Therefore, no considerations of spatial relationships in either atmosphere or ocean are taken during the AC procedure. When processing SeaWiFS data, Hu et al. (2000) showed that the aerosol type does not change significantly even in the 100–1000 km scale; therefore, aerosol properties derived in offshore clear waters could be applied to the adjacent turbid area. Acolite-DSF assumes homogeneous ρ_{path} for each tile within an OLI image, which is more stringent than assuming the aerosol type being uniform.

2.2. Atmospheric correction using multiple pixels in an image (MPACA)

2.2.1. Overview of the concept and assumptions

Unlike the conventional AC algorithms, this multi-pixel atmospheric correction approach utilizes the spatial relationship of aerosol properties from different pixels within one image in the AC process. The overall flowchart of MPACA is presented in Fig. 1. In particular, MPACA in its present form is designed to process turbid coastal waters for remote sensing measurements having at least two NIR or SWIR bands. Conceptually, MPACA is based on the assumption that the aerosol type does not change spatially for a small area (Gordon and Morel, 1983; Hu et al., 2000). Mathematically, MPACA is the same as the recent AC algorithm, which simultaneously solves both atmospheric and water properties (Two-angle Atmospheric Correction Algorithm, TAACA) from two sun-sensor geometries on the same day through spectral optimization (Wang et al., 2020). However, rather than using two geometries of the same pixel, MPACA uses two adjacent pixels within an HSR image to separate ρ_{path} from R_{rs} . The two adjacent pixels are determined by pairing a pixel (i.e., the target pixel) with another pixel (called the reference or contrast pixel) containing different water properties, whereas the atmospheric properties of both pixels are considered similar or highly related in order to constrain the mathematical solutions. Further, as in TAACA, the atmospheric contributions are modeled following POLYMER (Steinmetz et al., 2011), which adopted a polynomial function to simulate the atmospheric reflectance, rather than using LUTs adopted by the traditional AC approach to determine aerosol reflectance (Gordon, 1994; Gordon and Wang, 1994; Vanhellemont and Ruddick, 2018).

Mathematically, following Wang et al. (2020), ρ_t of the target pixel (represented as #1) and the reference pixel (represented as #2) can be expressed as:

$$\rho_{t,1}^{\text{mod}}(\lambda) = t_{g,1}(\lambda) \left[c_{0,1} + c_{1,1}(400/\lambda)^m + c_2(400/\lambda)^4 + t_{s,1}(\lambda)t_{v,1}(\lambda)\pi R_{rs,1}(\lambda) \right] \quad (2a)$$

$$\rho_{t,2}^{\text{mod}}(\lambda) = t_{g,2}(\lambda) \left[c_{0,2} + c_{1,2}(400/\lambda)^m + c_2(400/\lambda)^4 + t_{s,2}(\lambda)t_{v,2}(\lambda)\pi R_{rs,2}(\lambda) \right] \quad (2b)$$

In this expression, c_0 represents the contribution of sun glint and thin clouds. $c_1(400/\lambda)^m$ represents the contribution of aerosol scattering with parameter m characterizing the spectral variation of aerosol reflectance (with a default value as 1 (Steinmetz et al., 2011)). $c_2(400/\lambda)^4$ represents the sum of Rayleigh contribution and Rayleigh-aerosol coupled contributions (Wang et al., 2020). It should be noted that the sun glint contribution has a weak wavelength dependency and that c_1 and c_2

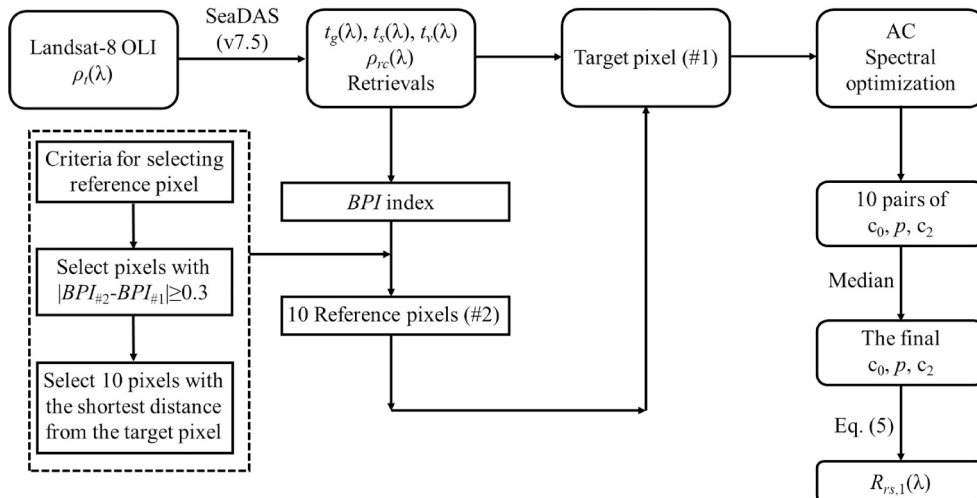


Fig. 1. Flowchart of MPACA to retrieve $R_{rs}(\lambda)$ from Landsat-8 OLI total reflectance at top-of-atmosphere.

implicitly compensated for its component during the optimization process. Further, we excluded the OLI images with strong sun glint.

The Rayleigh contribution is determined by three factors: atmospheric pressure, observational geometry, and ocean surface wind speed (Gordon et al., 1988; Gordon and Wang, 1992; Wang, 2005). For small areas considered in this study, the atmospheric pressure, wind speed, and the observation geometries corresponding to each pair of target and reference pixels are nearly identical. For instance, statistically, the difference in solar zenith angle and sensor viewing angle of each pair in this study is no more than 0.02° . Therefore, it is valid to assume parameter c_2 the same for the two pixels of each pair (see Section 2.2.2 for details).

As in TAACA (Wang et al., 2020), R_{rs} is calculated using an IOP-based remote-sensing reflectance model (R_{rs_IOPs}) (Lee et al., 1999) with three variables (P, G, X) representing the absorption coefficient of phytoplankton ($a_{ph}(440)$), the absorption coefficient of detritus and gelbstoff ($a_{dg}(440)$), and the backscattering coefficient of particles ($b_{bp}(440)$), all at 440 nm, respectively. This model has shown success in a wide range of applications covering oceanic, coastal and optically shallow waters (e.g., Ali et al., 2021; Dekker et al., 2011; Hu et al., 2006; Wei et al., 2020).

The required t_s and t_v for both pixels, which is related to aerosol type, AOD, Rayleigh optical depth (τ_r), and observational geometry, can be calculated with SeaDAS (v7.5) when processing a Landsat-8 OLI image. Since OLI has only one NIR band, as adopted in SeaDAS, a band in the SWIR domain is used for the derivation of AOD(865). To take advantage of decades of progress in ocean color remote sensing, MPACA uses the SeaDAS framework to process HSR data, where AOD(865), and then t_s and t_v , can also be retrieved for sensors with two NIR bands and no SWIR bands (e.g., SeaWiFS), although there could be different levels of uncertainties in the retrieved AOD(865).

In the TAACA system developed for processing VIIRS data over coastal waters, the value of m is treated as a variable to account for strongly absorbing aerosols over coastal regions. Here in MPACA, the value of m is fixed as 1.8, as it is the commonly encountered value for coastal waters (Wang et al., 2020). There are two reasons for adopting a fixed m value for processing Landsat-8 OLI: 1) To reduce the number of variables—The number of bands in the visible-NIR domain for Landsat-8 OLI is less than that for VIIRS, resulting in fewer equations from Landsat-8 OLI measurements; and 2) The shortest wavelength is 443 nm for Landsat-8 OLI, but a robust numerical resolution of m requires the availability of shorter blue bands, such as the 411 nm band of VIIRS. In the future, if a sensor has more bands in the blue wavelengths, a variable m could be adopted when there are strongly absorbing aerosols.

There are still eleven variables ($c_{0,1}, c_{0,2}, c_{1,1}, c_{1,2}, c_2, P_1, G_1, X_1, P_2, G_2, X_2$) for Eqs. (2a)–(2b), a further reduction of variables is required to obtain robust solutions for Landsat-8 OLI measurements when radiometric information in the 400–900 nm domain only is considered available. Since the distances between the target and reference pixels are relatively short, we may assume that the parameters $c_{0,1}$ and $c_{0,2}$ are also the same (then replaced as c_0 in the following). While the aerosol type and observational geometry for each pair of pixels are considered uniform, we allow variation in aerosol contributions between the two pixels. Since parameter c_1 is related to the aerosol optical depth at a reference wavelength (e.g., AOD(865)), we use the AOD(865) products to scale parameters $c_{1,1}$ and $c_{1,2}$, and they are expressed as:

$$c_{1,1} = p \times AOD(865)_1 \quad (3a)$$

$$c_{1,2} = p \times AOD(865)_2 \quad (3b)$$

where $AOD(865)_1$ and $AOD(865)_2$ are AOD(865) values for pixels #1 and #2, which are available from SeaDAS (v7.5) for a Landsat-8 OLI image. In short, if there are spatial variations in AOD(865), which will be reflected in the derived c_1 value. Thus, compared to Acolite-DSF, MPACA allows some spatially varying aerosol contributions within a Landsat-8 OLI image, although the aerosol type is assumed the same for the entire (sub)scene.

After the above considerations, the number of variables for Eqs. (2a)–

(2b) dropped to nine ($c_0, p, c_2, P_1, G_1, X_1, P_2, G_2, X_2$). Because the two pixels have different water properties and these variables impact an ρ_t spectrum differently, it is possible to solve these variables numerically by combining Eq. (2a) and Eq. (2b), similar to the spectral optimization scheme in TAACA. Fig. 2 shows examples of ρ_t spectra from a target pixel and a reference pixel, where large variations are present in the green-NIR wavelengths. We adopt a cost function err similar to that in Wang et al. (2020) to quantify the difference between the two sets of modeled and measured- ρ_t spectra:

$$err = \frac{\sqrt{\frac{\sum_{443}^{865} (\rho_{t,1}^{mea} - \rho_{t,1}^{mod})^2}{5} + \frac{\sum_{443}^{865} (\rho_{t,2}^{mea} - \rho_{t,2}^{mod})^2}{5}}}{\left(\frac{\sum_{443}^{865} \rho_{t,1}^{mea}}{5}\right) / 5 + \left(\frac{\sum_{443}^{865} \rho_{t,2}^{mea}}{5}\right) / 5} \quad (4)$$

where ρ_t^{mea} and ρ_t^{mod} refer to satellite measured and modeled ρ_t spectra, respectively. After values of c_0, p and c_2 are derived from spectral optimization, R_{rs} for the target pixel is calculated from Eq. (2a):

$$R_{rs,1}(\lambda) = \frac{\rho_{t,1}(\lambda) / t_{s,1}(\lambda) - [c_0 + p \times AOD(865)_1 \times (400/\lambda)^{1.8} + c_2(400/\lambda)^4]}{t_{s,1}(\lambda)t_{v,1}(\lambda)} \quad (5)$$

2.2.2. Detailed steps

The ultimate objective of MPACA is to accurately determine the atmospheric properties (c_0, p, c_2) of each target pixel within a Landsat-8 OLI image; then, R_{rs} of this pixel can be calculated from Eq. (5). During this process, as described above, a reference pixel (pixel #2) is required to constrain the atmospheric properties. For this reference pixel, it is necessary that 1) its distance from the target pixel should be small to ensure the assumption of the same aerosol type can be better satisfied; and 2) it needs to have different water properties from the target pixel, as the two equations would otherwise become one, preventing a robust mathematical solution. A process to select a suitable reference pixel is developed, which is described below.

- 1) An initial assessment of water optical properties before the sophisticated atmospheric correction was carried out. We adopt the black pixel index (BPI) (Wang et al., 2019) to classify the optical properties of a water pixel:

$$BPI = \frac{|\rho_{rc}(655) - \rho_{rc}(561)|}{\rho_{rc}(655) - \rho_{rc}(865)} \quad (6)$$

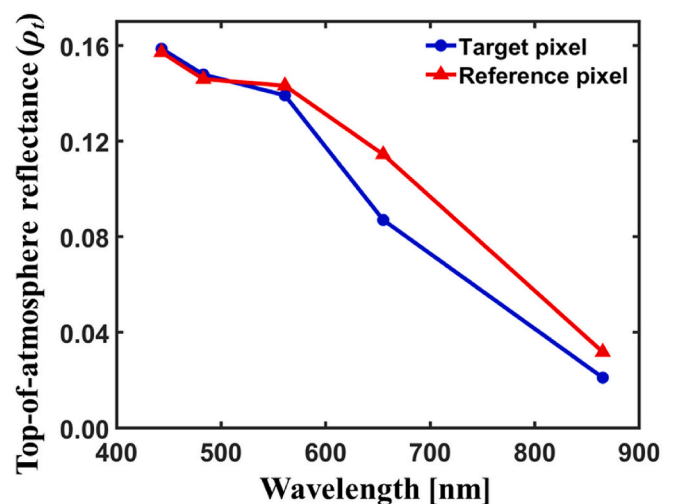


Fig. 2. The top-of-atmosphere reflectance ρ_t of a target pixel and a reference pixel from a Landsat-8 OLI image.

where ρ_{rc} is the Rayleigh-corrected reflectance. Based on BPI values, pixels are classified as “turbid” and “clear” waters. Through statistical analysis (see Fig. 3b), it is found that a value of $BPI = 1.0$ works well as the threshold, and less than 1.0 are classified as turbid waters.

- 2) After many trial-and-error experiments, it is found that as long as the BPI value of any pixel differs by an absolute value of 0.3 or larger from the BPI of the target pixel, this pixel can be considered to have different water properties. This will then form a pool of pixels having different water properties from that of the target pixel.
- 3) From the above pixel pool, 10 pixels with the shortest distance from the target pixel are then selected as the reference pixels (or pixel #2). Statistically, the average distance between the target pixel and the reference pixel is about 500 m.
- 4) Each of the 10 pixels is paired with the target pixel and then processed by the spectral optimization described above, resulting in ten sets of solutions for parameters c_0 , p , c_2 . The median values among the ten sets are selected as the final results for the target pixel, and then R_{rs} for the target pixel is calculated from Eq. (5).

For the optimization procedure, the MATLAB solver *fmincon* is employed to search for the minimum for Eq. (4). The optimization options include the maximum iterations as 100 and tolerance of 1×10^{-5} . The constraints for the optimization procedure are given in Table 1. The initial values for each unknown parameter are randomly chosen within the range of constraints.

3. Data

3.1. Satellite data and study areas

While MPACA is not tailored to a specific satellite sensor, we here use coastal measurements from Landsat-8 OLI to demonstrate its performance and applicability. Landsat-8 OLI has a spatial resolution of 30 m and five spectral bands in the 400–900 nm domain (centered at 443, 482, 561, 655, and 865 nm) (Franz et al., 2015a). Various studies have shown Landsat-8 OLI measurements as a valuable source to monitor water constituents in coastal and inland waters (Kuhn et al., 2019; Pahlevan et al., 2019; Vanhellemont and Ruddick, 2015; Wei et al., 2018).

For this study, the regions of Landsat-8 OLI measurements shown in Fig. 4 include Boston Harbor and Massachusetts Bay, Chesapeake Bay, Belgian coastal waters, and Long Island Sound.

- a) Boston Harbor and Massachusetts Bay (BH-MB) are located on the east coast of the United States. They are strongly impacted by winds,

hydrological environment, and other factors similar to other common semi-enclosed bays. Compared to Massachusetts Bay, the mean annual concentration of SPM over Boston Harbor varies from 3 to 8 mg L^{-1} (Taylor, 2016), which represents relatively turbid waters.

- b) The Chesapeake Bay (CB), alongside its tidal tributaries, is the largest estuary near Maryland and Virginia. The waters in the Chesapeake Bay are likewise impacted by tides, horizontal gradients driven by estuarine circulation, and freshwater contribution from rivers, which result in highly variable distributions of SPM, dissolved organic matter, and primary productivity (Cao et al., 2018a; Harding, 2015).
- c) The Belgian coastal waters, located in the southern North Sea with a depth of about 10 m in the nearshore region, are characterized by the occurrence of a coastal turbidity maximum (Fettweis et al., 2016; Fettweis et al., 2006). The concentration of SPM at the surface fluctuates from 20 to 250 mg L^{-1} . The port of Zeebrugge is situated in the maximum turbidity zone, where the water close to Zeebrugge is impacted by maintenance dredging work.
- d) Long Island Sound (LIS) is an elongated tidal estuary of the Atlantic Ocean, located in the north of Long Island, New York. The water optical properties around the AERONET-OC site LISCO are characterized by Chl-a $\sim 5 \text{ mg m}^{-3}$ and $\sim 2 \text{ mg L}^{-1}$ of SPM (Hlaing et al., 2010).

3.2. In situ data acquisition and match up

To validate the performance of MPACA for Landsat-8 OLI images, *in situ* measurements were assembled from multiple field campaigns (2013–2017) and four AERONET-OC sites (2013–2016). Six field campaigns were conducted over BH-MB and CB. Four AERONET-OC sites include COVE_SEAPRISM (SEAPRISM), Thornton_CPower (CPower), Zeebrugge_MOW1 (MOW1), and Long Island Sound Coastal Observatory (LISCO). The locations of *in situ* measurement stations are shown in Fig. 4, and the details of *in situ* measurements are briefly described below.

3.2.1. Ship-based measurements

The ship-based measurements contain five field campaigns conducted over BH-MB and one field campaign conducted over CB. The locations of *in situ* stations are denoted with red boxes in Figs. 4a and 4b. During each field campaign over BH-MB, *in situ* R_{rs} was measured following the skylight-blocked approach (SBA) (Lee et al., 2013). At each sampling station, two radiometric properties were measured with hyperspectral radiometers (HyperOCR, Satlantic Inc.): water-leaving radiance (L_w , $\text{W m}^{-2} \text{ nm}^{-1} \text{ sr}^{-1}$) and downwelling plane irradiance (E_d , $\text{W m}^{-2} \text{ nm}^{-1}$) in a spectral range from 349.7 to 804.6 nm with 137 spectral bands. R_{rs} was obtained following the same protocol as Wei

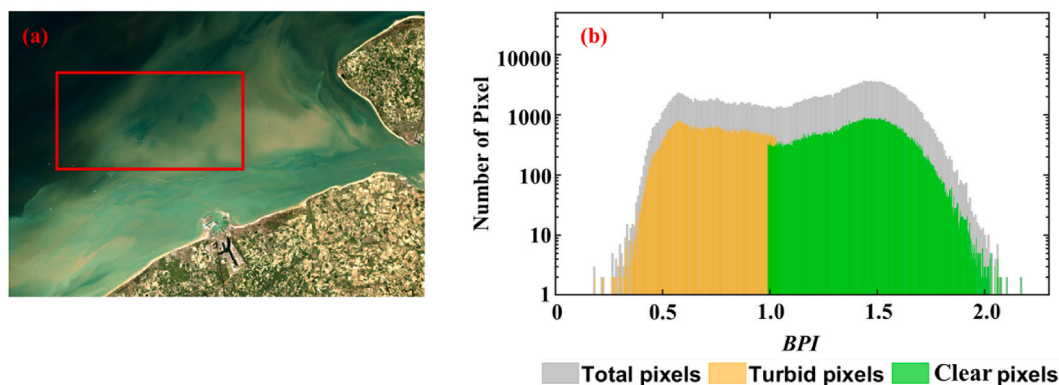


Fig. 3. (a) True color image for the port of Zeebrugge and offshore waters situated on the coast of Belgium from Landsat-8 OLI on April 1st, 2014. (b) Histogram distribution for the BPI index of water pixels where the label “Total pixels” represents all pixels in the red box of Fig. 3a, and the label “Turbid pixels” and “Clear pixels” are, respectively, the turbid and clear water pixels classified based on the BPI value. (For interpretation of the references to color in this figure legend, the reader is referred to the web version of this article.)

Table 1

Range for both atmospheric and oceanic parameters in the process of MPACA, where Min. and Max. represent the lower and upper boundaries of these parameters, respectively.

	c_0	p	c_2	P_1 (m^{-1})	G_1 (m^{-1})	X_1 (m^{-1})	P_2 (m^{-1})	G_2 (m^{-1})	X_2 (m^{-1})
Min.	1×10^{-7}	0.0001	0.0001	0.005	0.002	0.001	0.005	0.002	0.001
Max.	0.1	1.0	1.5	2.5	3.0	1.0	2.5	3.0	1.0

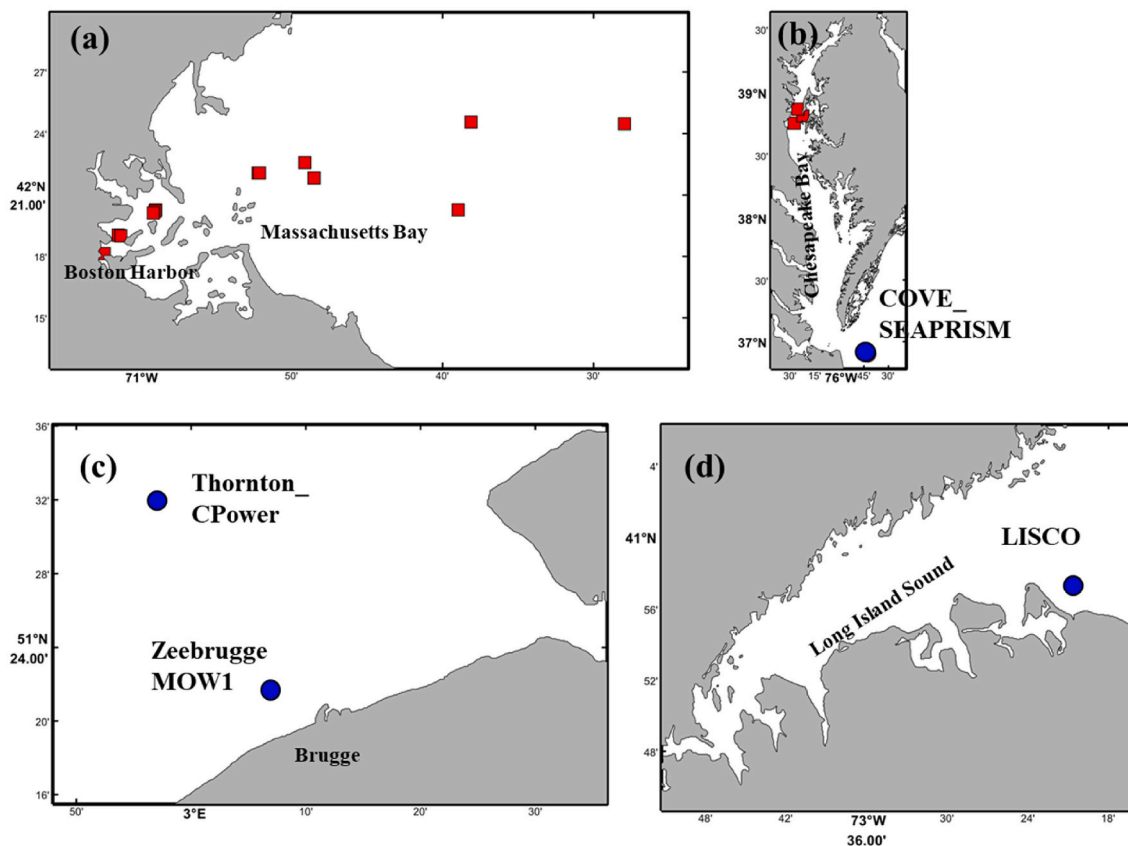


Fig. 4. Locations of *in situ* measurements used in this study. (a) Massachusetts Bay and Boston Harbor; (b) the Chesapeake Bay; (c) Belgian coast and (d) Long Island Sound, with the sampling stations collected from six field campaigns ($n = 16$, red boxes) and four AERONET-OC sites (COVE_SEAPRISM, Thornton_CPower, Zeebrugge MOW1, and LISCO, $n = 22$, blue dots), with 38 stations in total. (For interpretation of the references to color in this figure legend, the reader is referred to the web version of this article.)

et al. (2018). The data for the field measurements in the Chesapeake Bay were downloaded from SeabASS maintained by the NASA Ocean Biology Processing Group (OBPG) (<https://seabass.gsfc.nasa.gov/ssearch/>), where the R_{rs} were calculated from measurements using GER 1500 spectroradiometer, designed to gather fast spectral measurements from ~ 350 to 1050 nm at ~ 3 nm resolution.

The hyperspectral R_{rs} spectrum from field measurements was spectrally convoluted to the corresponding R_{rs} data at the five Landsat-8 OLI visible-NIR bands with Landsat-8 OLI's spectral response function (Pahlevan et al., 2014):

$$R_{rs}^{LS}(B_i) = \frac{\int_{400}^{900} R_{rs}(\lambda) RSR_i(\lambda) d\lambda}{\int_{400}^{900} RSR_i(\lambda) d\lambda} \quad (7)$$

where RSR_i represents the response function of band B_i . The full spectra RSR of Landsat-8 OLI can be accessed online (Ball_BA_RSR.v1.11).

3.2.2. AERONET-OC measurements

We also acquired twenty-two cloud-screened and fully quality-controlled Level 2.0 AERONET-OC measurements of normalized

water-leaving radiance (L_{wn}) from four AERONET-OC sites at SEAPRISM, CPower, MOW1, and LISCO. SEAPRISM, MOW1, and LISCO are located in coastal nearshore waters, while CPower is situated further offshore in relatively clearer waters (see Figs. 4b–4d, blue dots).

AERONET-OC is an extended network from AERONET developed by the National Aeronautics and Space Administration (NASA) for marine applications. By installing the modified sun-photometers on offshore platforms worldwide, AERONET-OC provides *in situ* radiometric measurements over a water body (*i.e.*, water-leaving radiance) (Holben et al., 1998; Holben et al., 2001; Zibordi et al., 2009). Level 2.0 Quality Assured L_{wn} ($mW\ cm^{-2}\ \mu m^{-1}\ sr^{-1}$) from AERONET-OC was downloaded from the AERONET website (<http://aeronet.gsfc.nasa.gov/>), which was further converted to R_{rs} through the following formula:

$$R_{rs}(\lambda) = \frac{L_{wn}(\lambda)}{F_0(\lambda)} \quad (8)$$

For SEAPRISM, CPower, and LISCO sites, an f/Q correction of the bidirectional effects (Morel et al., 2002) was implemented for the generation of L_{wn} . For MOW1, however, there was no f/Q correction for L_{wn} , as the Chl-a based f/Q correction scheme is not adequate for this turbid

site (Zibordi et al., 2009).

Separately, there is a relatively large difference in the center wavelengths, *i.e.*, 8 to 12 nm, between AERONET-OC (443, 490, 551, and 667 nm) and Landsat-8 OLI (443, 482, 561, 655 nm), except for the 443 nm band. In order to obtain a consistent evaluation, the AERONET-OC R_{rs} bands need to be shifted to the Landsat-8 OLI bands. For this conversion, the large (~800) hyperspectral R_{rs} dataset in Lee et al. (2014) was analyzed, and significant linear relationships among three-band pairs of R_{rs} , *i.e.*, 490 nm vs 482 nm, 550 nm vs 560 nm, and 665 nm vs 655 nm, were obtained (see Fig. 5). Therefore, these relationships were applied to convert the R_{rs} of AERONET-OC band to Landsat-8 band before the evaluation of OLI R_{rs} . Note that before establishing the above relationships, as described above (see Eq. (7)), the hyperspectral R_{rs} were spectrally convoluted to the corresponding R_{rs} data at the four OLI visible bands.

3.3. Method of evaluation and statistical metrics

For subsequent analysis, the satellite pixels with substantial cloud contamination were identified and discarded. Meanwhile, for the retrievals (*i.e.*, $R_{rs}(\lambda)$, $t_s(\lambda)$, $t_p(\lambda)$, *etc.*) from SeaDAS, the pixels with low-quality retrievals were also removed based on the standard Level-2 quality flags, which include ATMFAIL (Atmospheric correction failure), LAND (land pixel), CLDICE (Probable cloud or ice contamination), HILT (very high or saturated observed radiance) and HIGLINT (Strong sun glint contamination).

To minimize the effects of temporal and spatial mismatches between the satellite and *in situ* data for ship-based measurements, we adopt a time constraint of ± 1.5 h to create *in situ* and satellite matchups. As a result, sixteen sampling stations were matched between Landsat-8 OLI and *in situ* ship-based measurements, with thirteen stations in BH-MB (Fig. 4a, red boxes) and three stations in CB (Fig. 4b, red boxes). The Landsat-8 images used for this comparison are listed in Table S1 of the Supplementary Information available online. For each matching field station for all four AC algorithms analyzed here, we also excluded data where the coefficient of variation (CV) within a 3×3 box of the OLI image surrounding the location of *in situ* stations is greater than 0.15.

For matchups between AERONET-OC and Landsat-8 OLI, the allowed maximum time difference between Landsat-8 OLI overpass and the measurement time of AERONET-OC data was also set to ± 1.5 h. When more than one AERONET-OC measurement satisfied this criterion, the AERONET-OC measurements were linearly interpolated to the corresponding satellite overpass time based on the measurement time of AERONET-OC data. Finally, we obtained a total of twenty-two matchups between Landsat-8 OLI and *in situ* data for the four AERONET-OC sites (Fig. 4b–d, blue dots). Information of aerosol optical depth, solar zenith angle (SZA), and wind speed (m s^{-1}) for each matchup is also available. The Landsat-8 OLI images for this comparison are listed in Table S2 of the Supplementary Information available online. For the satellite images, the median R_{rs} values within a box of 7×7 pixels centered on the AERONET-OC station were used for the evaluations to exclude additional noise resulting from the station or its shadow.

To quantitatively measure the performance of each AC approach, we calculated the coefficient of determination (R^2), the Mean Absolute Percentage Difference (MAPD), bias and the Root Mean Square Difference (RMSD) between the results from atmospherically corrected OLI image (Q_{sat}) and *in situ* measured R_{rs} (Q_{mea}),

$$MAPD = \frac{1}{N} \times \sum_{i=1}^N \left| \frac{Q_{sat,i} - Q_{mea,i}}{Q_{mea,i}} \right| \times 100\% \quad (9a)$$

$$Bias = \frac{1}{N} \times \sum_{i=1}^N (Q_{sat,i} - Q_{mea,i}) \quad (9b)$$

$$RMSD = \sqrt{\frac{1}{N} \times \sum_{i=1}^N (Q_{sat,i} - Q_{mea,i})^2} \quad (9c)$$

where $Q_{sat,i}$ and $Q_{mea,i}$ refer to satellite products and *in situ* measurements, respectively, and N the number of data pairs.

4. Results and discussions

4.1. Evaluation of existing AC algorithms with *in situ* measurements

We first evaluated the performance of a few widely used AC algorithms with all matchup measurements. Fig. 6 shows a comparison between *in situ* R_{rs} and Landsat-8 OLI R_{rs} (bands 443–655 nm) retrieved by SeaDAS (blue), Acolite-DSF (yellow), and Acolite-EXP (red), respectively, for all the matchup sampling stations ($N = 38$), with detailed statistical evaluations presented in Table 2. Generally, among the three AC approaches, the R_{rs} retrieved by SeaDAS (R_{rs}^{SeaDAS}) matched best with *in situ* R_{rs} (R_{rs}^{insitu}), where the R^2 value of each band for all the evaluation data is above 0.91 (Table 2), with RMSD value varying from 0.0010 sr^{-1} (655 nm) to 0.0018 sr^{-1} (482 nm), and MAPD from 13.8% (561 nm) to 38.8% (443 nm) (see Table 2). The retrieved R_{rs}^{SeaDAS} shows better accuracy at 561 and 655 nm, with RMSD of 0.0017 sr^{-1} and 0.0010 sr^{-1} , and MAPD of 13.8% and 25.6%, respectively. The larger deviations of R_{rs}^{SeaDAS} at 443 nm and 482 nm happened at the AERONET-OC site MOW1, where $R_{rs}(443)$ was in a range of $0.010\text{--}0.015 \text{ sr}^{-1}$, indicating challenges in processing turbid waters. There are a few negative R_{rs}^{SeaDAS} values at 443 nm for stations located in Boston Harbor, which may be resulted from the impact of absorbing aerosols as reported before (Bailey and Werdell, 2006; Hlaing et al., 2013; Hu et al., 2019), with these pixels flagged by the 12_flag “ABSAER”.

For this dataset, the R^2 value for the retrieved $R_{rs}(\lambda)$ by Acolite-DSF is comparable with that of SeaDAS $R_{rs}(\lambda)$ at the four visible bands, but the MAPD of the retrieved R_{rs} from DSF (R_{rs}^{DSF}) at each band is about two times that of R_{rs}^{SeaDAS} . The larger deviation over MB-BH could be that the ρ_{path} is not completely uniform over certain tiles. The specific reasons for these results need to be further analyzed, which is beyond the scope of this study.

In contrast, Acolite-EXP exhibits less satisfactory results, especially in the blue bands (see Fig. 6). The Acolite-EXP generally overestimates $R_{rs}(\lambda)$ at all the visible bands, especially for $R_{rs}(443)$ (in a range of

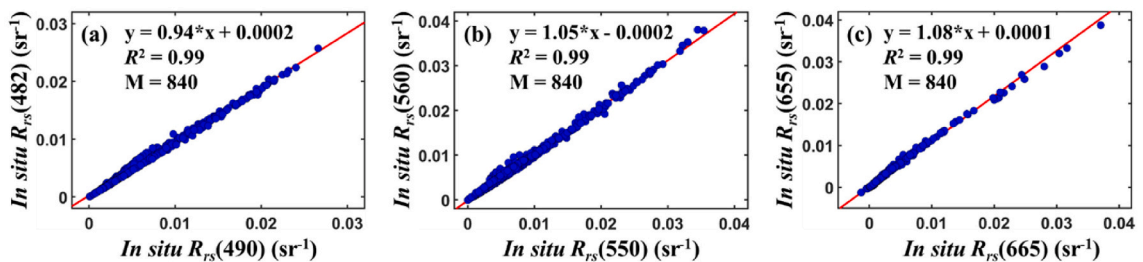


Fig. 5. Scatterplot comparisons between $R_{rs}(490)$ and $R_{rs}(482)$, $R_{rs}(550)$ and $R_{rs}(560)$, and $R_{rs}(665)$ and $R_{rs}(655)$ for *in situ* hyperspectral R_{rs} dataset in Lee et al. (2014). R_{rs} of Landsat-8 OLI bands were spectrally convoluted with OLI's band response functions.

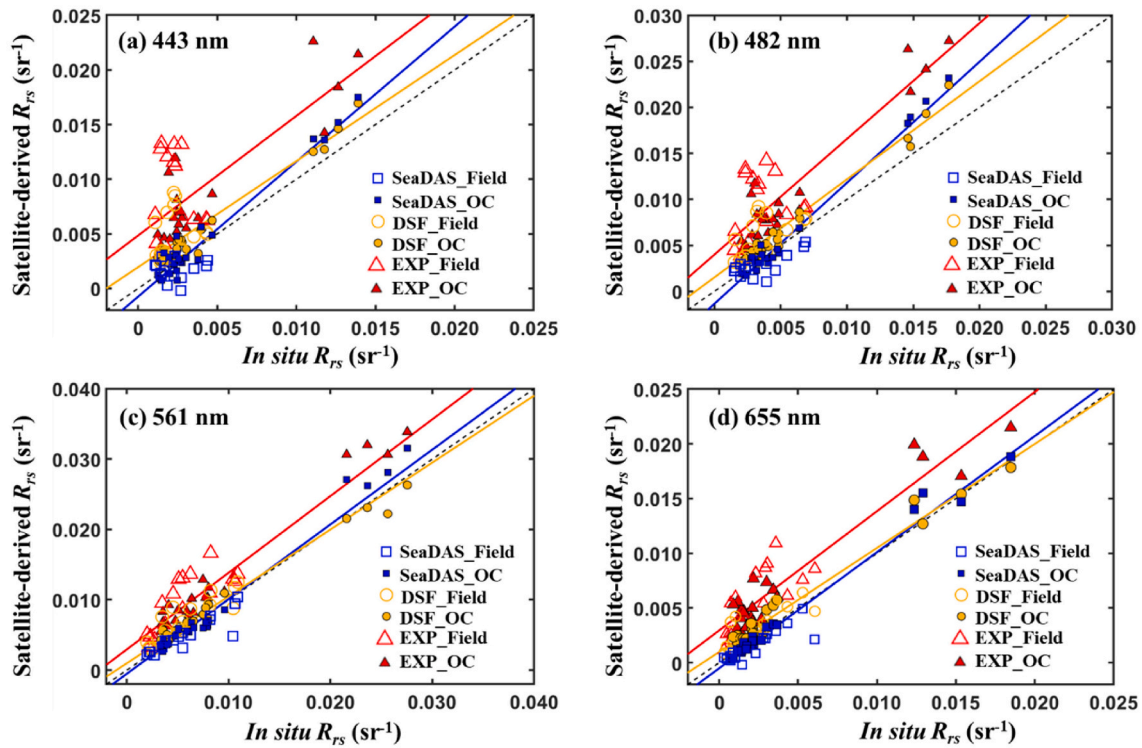


Fig. 6. Scatterplot comparison between Landsat-8 OLI-derived R_{rs} and *in situ* R_{rs} at Landsat-8 each visible band from SeaDAS, Acolite-DSF, and Acolite-EXP. The black dash line represents the 1:1 line. The different color solid lines represent the linear regression for different AC algorithms corresponding to all matchups, respectively (blue line for SeaDAS, yellow line for Acolite-DSF, and red line for Acolite-EXP). “Field” and “OC” represent the *in situ* R_{rs} from the field campaigns (open symbols) and AERONET-OC sites (solid symbols), respectively. (For interpretation of the references to color in this figure legend, the reader is referred to the web version of this article.)

Table 2

Statistics for all matchup sampling stations of R_{rs} at each visible wavelength derived from SeaDAS, Acolite-DSF, Acolite-EXP and MPACA approaches, respectively, for Landsat-8 measurements.

Band	Scheme	N	R^2	Slope ^a	Int ^a	RMSD (sr ⁻¹)	MAPD (%)	Bias (sr ⁻¹)
443	SeaDAS	38	0.91	1.24	-0.0007	0.0014	38.8	0.00006
	Acolite-DSF	38	0.79	0.97	0.0019	0.0024	89.1	0.0018
	Acolite-EXP	38	0.53	1.10	0.0048	0.0062	228.2	0.0052
	MPACA	38	0.98	0.97	0.00004	0.0004	10.2	-0.00005
482	SeaDAS	38	0.95	1.32	-0.0014	0.0018	23.5	0.0002
	Acolite-DSF	38	0.9	1.07	0.0015	0.0023	54.0	0.0018
	Acolite-EXP	38	0.76	1.26	0.0040	0.0061	146.1	0.0053
	MPACA	38	0.99	0.98	0.00004	0.0005	8.7	-0.00007
561	SeaDAS	38	0.96	1.15	-0.0013	0.0017	13.8	-0.0002
	Acolite-DSF	38	0.96	0.87	0.0019	0.0017	26.2	-0.0008
	Acolite-EXP	38	0.93	1.15	0.0028	0.0046	69.0	0.0040
	MPACA	38	0.99	1.06	-0.0003	0.0006	6.6	0.0001
655	SeaDAS	38	0.96	1.06	-0.0005	0.0010	25.6	-0.0003
	Acolite-DSF	38	0.95	0.95	0.0010	0.0012	63.4	0.0008
	Acolite-EXP	38	0.87	1.09	0.0030	0.0037	185.0	0.0033
	MPACA	38	0.98	1.06	-0.0002	0.0006	16.2	0.00001

^a Slope and Int are the slope and intercept of the fitting line, respectively.

~0.002–0.015 sr⁻¹), where the RMSD and MAPD values are as high as 228% and 0.0062 sr⁻¹, respectively (see Fig. 6 and Table 2). This kind of overestimation was also reported in Vanhellemont (2019) and Xu et al. (2020).

The contrasting performance among SeaDAS, Acolite-DSF and Acolite-EXP is further manifested by comparing the overall shapes and ranges between *in situ* R_{rs} and satellite-retrieved R_{rs} spectra for the six locations (see Fig. 7). Separately, the R_{rs} spectra from SeaDAS show similar spectral shapes and ranges compared to R_{rs} from *in situ* measurements for the six locations. Except for MB, the spectral shapes of the retrieved R_{rs} by Acolite-DSF for the other five locations are also similar

to that of R_{rs}^{insitu} , but the values of the mean R_{rs}^{DSF} are much higher than that from R_{rs}^{SeaDAS} over BH, CB, and LISCO (Figs. 7a, 7e and 7f). In contrast, Acolite-DSF shows better performance over MOW1 and CPower compared to SeaDAS, which is also reported in Ilori et al. (2019) and Vanhellemont (2020).

4.2. Evaluation of MPACA with *in situ* measurements

Like the above, we evaluated the performance of MPACA using *in situ* measurements, with Fig. 8 showing scatterplots between measured and MPACA-retrieved R_{rs} , and the statistical measures included in Table 2.

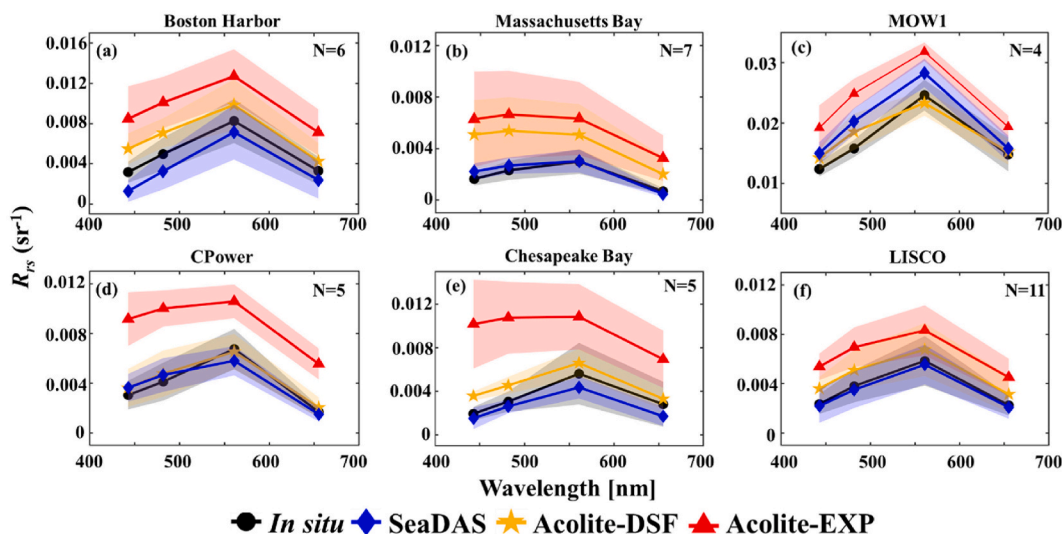


Fig. 7. Qualitative comparison of *in situ* R_{rs} measurements against SeaDAS, Acolite-DSF and Acolite-EXP retrieved R_{rs} for Boston Harbor (a), Massachusetts Bay (b), AERONET-OC site “MOW1” (c), AERONET-OC site “CPower” (d), Chesapeake Bay (e) and AERONET-OC site “LISCO” (f). Solid lines are the average reflectance spectra for all matchups, while shaded regions are one standard deviation from the average.

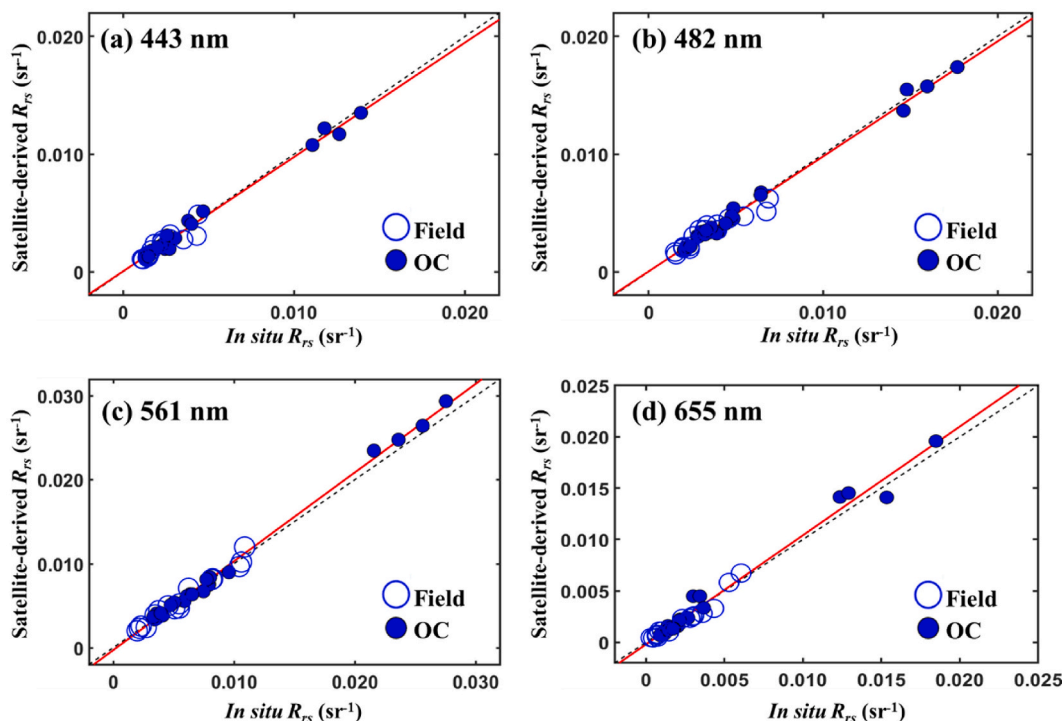


Fig. 8. Same as Fig. 6, but for results of MPACA.

Overall, the R^2 value is ~ 0.98 or better for each OLI band. Compared to SeaDAS, MPACA reduced the MAPD by a factor of three for the two blue bands, from 38.8% to 10.2% at 443 nm, and from 23.5 to 8.7% at 482 nm (see Table 2). The higher R^2 , lower RMSD and MAPD values in all the OLI bands indicate excellent agreement of R_{rs} between MPACA retrievals and *in situ* measurements. This agreement is also manifested in Fig. 9, where the mean and the range of R_{rs} spectra from MPACA match very well with those from *in situ* measurements for the six locations, even though each location is associated with a different load of water constituents and each Landsat-8 OLI image contains different atmospheric properties. It is worth noting that the ranges of R_{rs} at 561 nm and 655 nm over the Chesapeake Bay (Fig. 9e) are larger than those of the other five

regions. The reason is that the *in situ* R_{rs} of this region came from two regions with relatively different water optical properties, with one in the upper section of the bay and the other at the mouth of the bay.

It is necessary to point out that MPACA, TAACA, and POLYMER included an R_{rs} model with spectral modeling of IOPs in the process, which provides additional constraints to R_{rs} spectrum, therefore, more reasonable and accurate R_{rs} spectra could be expected for such approaches compared to SeaDAS. Because of the spectral optimization, however, it takes a much longer time for MPACA to process an image than SeaDAS. At present, after retrieving AOD, t_s and t_v via SeaDAS, it takes ~ 5 h to process an OLI image of a size ~ 90 km \times 40 km with a personal computer (Intel(R) Core(TM) i7-10700F CPU @ 2.90 GHz,

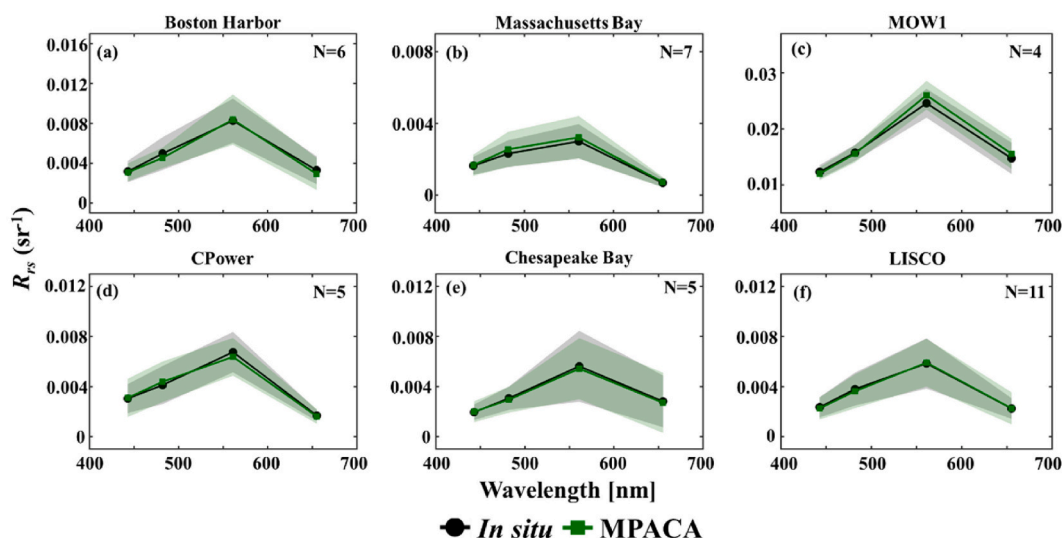


Fig. 9. Same as Fig. 7, but for results of MPACA.

Hacker God DDR4 3200 16G RAM and ASUS 1060S 6G graphics card). The use of more robust computer configurations or supercomputers should be able to improve the computation efficiency of this algorithm.

4.3. Relationship between the performance of AC algorithms and environmental conditions

Although the above results indicate that MPACA is a promising alternative of atmospheric correction for processing HSR data (having at least two bands in the NIR or SWIR domain) in coastal regions, there are still differences between MPACA retrievals and *in situ* measurements. To see if any specific relationships exist between the remaining uncertainties and environmental parameters, we analyzed the performance of MPACA and some other algorithms for a few key environmental conditions.

4.3.1. Performance of MPACA over turbid coastal waters

As shown in the literature and Fig. 6, it is always a challenge to

accurately remove atmospheric contributions in turbid coastal waters, with errors mainly due to inaccurate estimations of $R_{rs}(NIR)$ (IOCCG, 2010). The commonly applied AC algorithms usually extend the “black pixel” assumption from NIR to SWIR bands to better ensure negligible water-leaving radiance in the measured signal (IOCCG, 2010; Wang and Shi, 2007), a strategy applicable only to sensors with two or more highly-sensitive SWIR bands. However, MPACA in its design is for sensors with limited SWIR bands (need at least two NIR or SWIR bands) such that it has a broader range of applicability to satellite measurements. Therefore, it is necessary to evaluate the performance of MPACA over turbid coastal waters. Fig. 10 shows a subset OLI “true color” RGB image of 2014-04-01 over Belgian coastal waters, where high concentrations of SPM are shown as bright brownish patches. For instance, the submerged sand dune and advection of small-scale sediment in and around the port of Zeebrugge show high SPM concentration (Fig. 10). Because of the high spatial resolution (30 m) of the Landsat-8 OLI image, the offshore construction of CPower wind farm, large ships and their turbid wakes are also revealed (Fig. 10). The spatial distributions of OLI-



Fig. 10. Rayleigh corrected RGB (655, 561 and 482 nm) Landsat-8 OLI image over Belgian coastal waters on April 1st, 2014, showing turbid coastal waters with high concentrations of suspended particulate matter (yellow-brown). (For interpretation of the references to color in this figure legend, the reader is referred to the web version of this article.)

derived R_{rs} at 443, 482, 561, 655, and 865 nm by MPACA (left column) and SeaDAS (right column), respectively, for this subset image, are shown in Fig. 11.

For this turbid environment, we compared R_{rs} from MPACA and SeaDAS (where one SWIR and one NIR bands were used in the atmospheric correction process) with that from AERONET-OC measurements, with results showing in Figs. 11 and 12. Overall, similar spatial patterns of the retrieved R_{rs} at the five visible-NIR bands are revealed between results from MPACA and those from SeaDAS (R^2 values generally > 0.82 , see Fig. 12), although the values of R_{rs}^{MPACA} are relatively lower than that of R_{rs}^{SeaDAS} . Generally, the best agreement between R_{rs}^{MPACA} and R_{rs}^{SeaDAS} is found at 561 nm and 655 nm (Figs. 12c and 12d), while $R_{rs}^{MPACA}(865)$ is lower by $\sim 40\%$ compared to $R_{rs}^{SeaDAS}(865)$ (Fig. 12e). To gain more insights into these comparisons, we compared the spectra of R_{rs}^{MPACA} , R_{rs}^{DSF} and R_{rs}^{SeaDAS} with the R_{rs} obtained from the AERONET-OC site-MOW1 on 2014-4-1 (Fig. 12f). It is found that, in general, they all agree with each other very well in spectral shape, but the R_{rs} values from MPACA are closer (4.5% difference on average) to that from *in situ* measurements, whereas the values from SeaDAS and Acolite-DSF are relatively higher (16.3% and 19.8% on average, respectively) than *in situ* values, especially at blue bands. In particular, for $R_{rs}(865)$, the *in situ* value is about 0.0023 sr^{-1} , but it is 0.0025 sr^{-1} from SeaDAS, 0.0033 sr^{-1} from Acolite-DSF and 0.0022 sr^{-1} from MPACA. Although they are generally similar (except Acolite-DSF), these

values suggest that the lower values from MPACA are more consistent with those from AERONET-OC measurements, at least for this image. These comparisons and evaluations indicate that MPACA can obtain valid R_{rs} over turbid coastal waters for satellites with at least two bands in the NIR or SWIR domain. However, similar to the development of all algorithms, more evaluations of MPACA are necessary in the future, especially over highly turbid waters where likely a more suitable model for R_{rs} and a more accurate algorithm for retrieving AOD might be required.

4.3.2. Sensitivity of MPACA to the accuracy of AOD(865)

One of the basic assumptions for the proposed MPACA is that the aerosol type is uniform in a relatively small region, while the aerosol load could vary following AOD(865). For turbid coastal waters, the retrieved AOD(865) value from NASA SeaDAS is not error-free (Gordon and Wang, 1994; IOCCG, 2010), which will subsequently introduce errors in the spatial relationship between the target pixel and reference pixel (see Eqs. (3a), (3b)). Further, as t_s and t_r are weakly dependent on AOD (Gordon and Morel, 1983; Ma et al., 2006; Wang, 1999), errors in the estimation of AOD(865) will likely be further propagated to the retrieval of R_{rs} . Here, to characterize the potential effect of the accuracy of AOD(865) on the retrieval of R_{rs} by MPACA, for all the evaluation stations, sensitivity tests were carried out by adding errors to the values of AOD₁ (the AOD(865) product of the target pixel) and AOD₂ (the AOD(865) product of the reference pixel). Note that for these stations, the range of retrieved-AOD₁ from SeaDAS (with one NIR band and one SWIR band) is ~ 0.02 to ~ 0.2 , a range quite large for valid ocean color remote sensing, although the range of ~ 0.02 to ~ 0.1 contributes to 79% of all the evaluation stations (see Fig. 13a). Separately, Fig. 13b shows a scatterplot of AOD₁/AOD₂ for all the evaluation stations, which indicates the spatial variation of aerosol load and potentially variations of water optical properties. For these sensitivity tests, $\pm 50\%$ errors (i.e., assumed the largest error as 50%) were added to the original AOD₁ and AOD₂ values (eight different combinations). Further, for each combination of AOD₁ and AOD₂, the corresponding t_s and t_r of both pixels were modeled following Gordon and Morel (1983), which is a function of aerosol optical depth, Rayleigh optical depth, single-scattering albedo, aerosol phase function, and observational geometry (see Supplementary Information for details).

Fig. 14 shows a comparison of R_{rs} at all visible bands, for the entire evaluation datasets (both field measurements and AERONET-OC), between the MPACA retrievals and *in situ* measurements after adding $\pm 50\%$ errors to AOD₁ and AOD₂, where AOD_{1,test} and AOD_{2,test} refer to error-added AOD₁ and AOD₂, respectively, with detailed statistical evaluations for each visible band presented in Table 3. Overall, the R^2 values are all ~ 0.98 and the slopes of linear regressions all approach the 1:1 line (slopes vary from 0.97 to 1.03) for these combinations. Further, for these cases, the overall RMSD values are less than $\sim 0.007 \text{ sr}^{-1}$ and the overall MAPD values less than 13.0%, comparable to those obtained with the original AOD(865) values. The highest MAPD (12.6%) corresponds to the case where, at the same time, AOD_{1,test}/AOD₁ is 0.5 while AOD_{2,test}/AOD₂ is 1.5 or AOD_{1,test}/AOD₁ is 1.5 while AOD_{2,test}/AOD₂ is 0.5, a situation that is rare to happen. Meanwhile, for each visible band, its values of RMSD and MAPD are comparable to that across all the spectral bands (see Table 3). These results indicate the negligible impact of errors in AOD(865) (at least for errors no more than 50%) on the retrieval of R_{rs} . The reason for such insensitivity is partly due to that AOD(865) is simply an initial value used in MPACA to constrain its spatial variations, where the final contribution from the aerosol and atmospheric path radiance is determined through spectral optimization.

We further evaluated the spectral similarity between the MPACA-retrieved and *in situ* R_{rs} spectra using a cosine mapper:

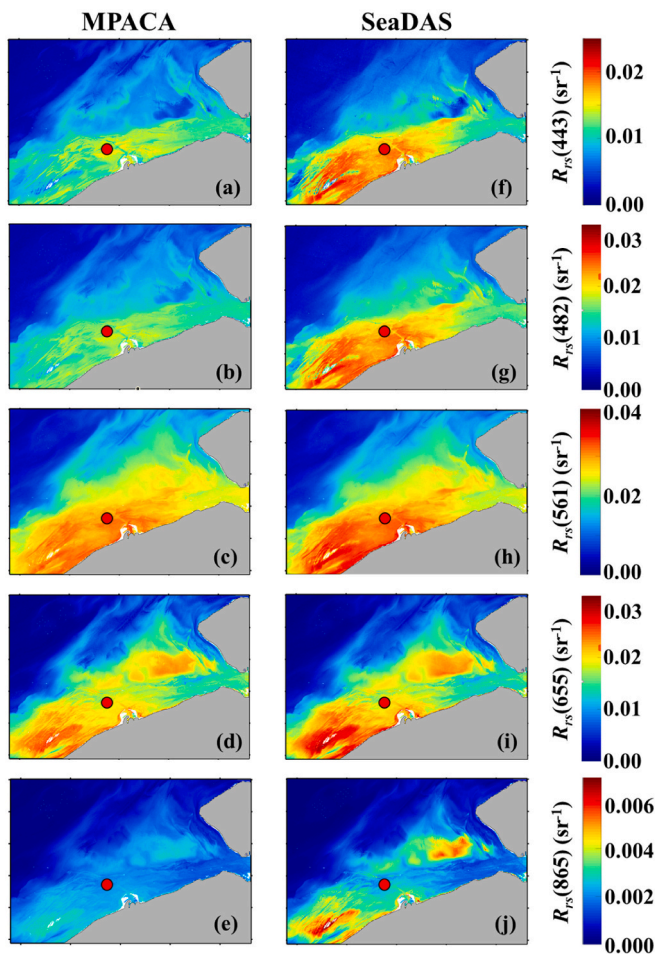


Fig. 11. The spatial distribution of $R_{rs}(443)$, $R_{rs}(482)$, $R_{rs}(561)$, $R_{rs}(655)$, and $R_{rs}(865)$ over Belgian coastal waters for Landsat-8 OLI image on April 1st, 2014, retrieved by MPACA (left row) and SeaDAS (right row). The red dot is the location of the AERONET-OC site-MOW1. (For interpretation of the references to color in this figure legend, the reader is referred to the web version of this article.)

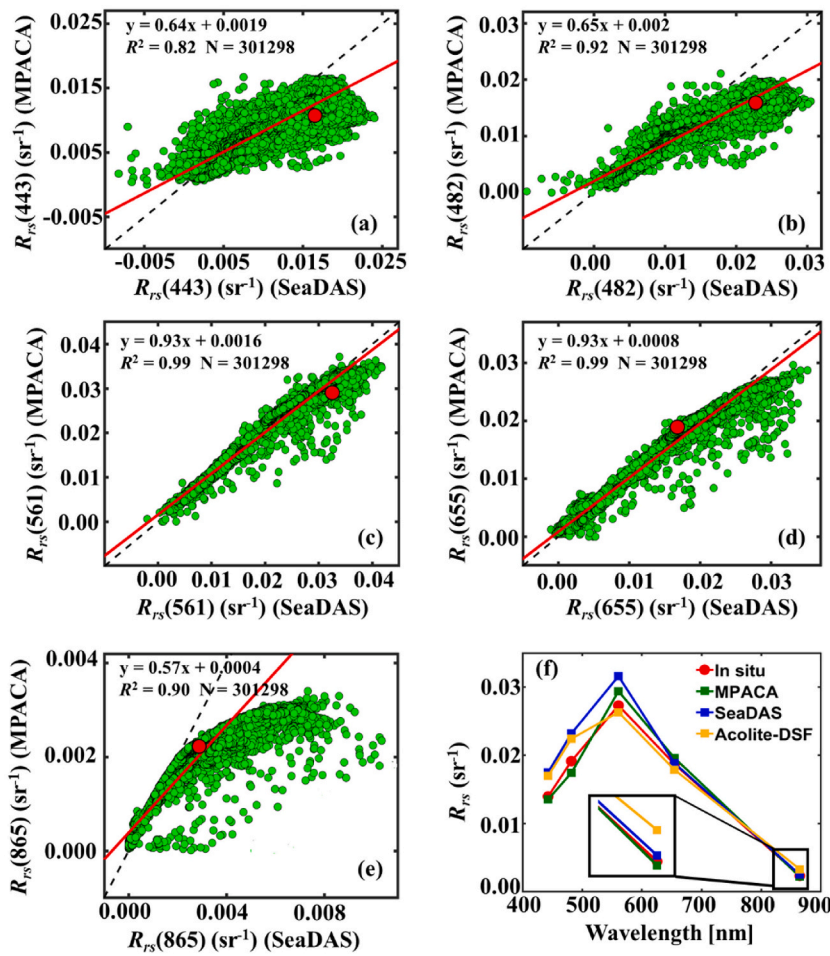


Fig. 12. (a–e) The comparisons between R_{rs} at 443, 482, 561, 655 and 865 nm derived from SeaDAS (x-axis) and MPACA (y-axis), respectively, for 2014-04-01 Landsat-8 OLI image over Belgian coastal waters. The dashed black line is 1:1 line, and the solid red line is the linear regression. The red dots represent the R_{rs} values retrieved by MPACA and SeaDAS for AERONET-OC site-Zeebrugge_MOW1 on this day. (f) R_{rs} spectra of *in situ* measurement (red line), Landsat8 OLI-derived by MPACA (green line), SeaDAS (blue line) and Acolite-DSF (yellow line) method for AERONET-OC site-Zeebrugge_MOW1 over Belgian coastal waters on April 1st, 2014. The NIR spectral region is magnified in a small box. (For interpretation of the references to color in this figure legend, the reader is referred to the web version of this article.)

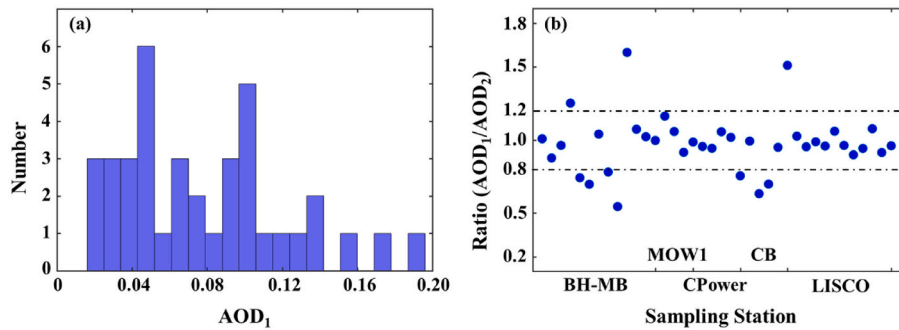


Fig. 13. (a) Distributions of SeaDAS (v7.5) retrieved AOD(865) (for pixel #1) from Landsat-8 measurements for all the evaluation stations ($N = 38$). (b) A scatterplot of the ratio between the AOD(865) products of the target pixel (AOD₁) and reference pixel (AOD₂) for all the evaluation stations.

$$\cos(\alpha) = \frac{\sum_{i=1}^N Rrs_{sat,i} Rrs_{mea,i}}{\sqrt{\sum_{i=1}^N (Rrs_{sat,i})^2} \sqrt{\sum_{i=1}^N (Rrs_{mea,i})^2}} \quad (10)$$

with α the angle between the *in situ* R_{rs} (Rrs_{mea}) and the satellite-retrieved R_{rs} (Rrs_{sat}) spectra. The higher the spectral similarity between the two spectra, the smaller the angle α . For each error combination, the α value is close to 0, indicating that the R_{rs} spectra from MPACA with error-added AOD(865) have a very high spectral consistency with *in situ* R_{rs} . All above evaluations suggest that MPACA can tolerate errors in AOD(865) to at least ~50%.

As described earlier, one of the basic assumptions for the proposed MPACA is that the aerosol type is uniform in a relatively small region. However, the aerosol type could be different even for small images in size like Landsat-8 OLI under the influence of wind, which plays a vital role in mixing and advecting aerosol (André and Morel, 1991). For such exceptional situations, it might be necessary to evaluate the aerosol types in the study area, and a pixel-dependent parameter m might be required. More efforts are needed in the future to address measurements with significant variations of aerosol types.

5. Conclusions

In this effort, we have developed an atmospheric correction

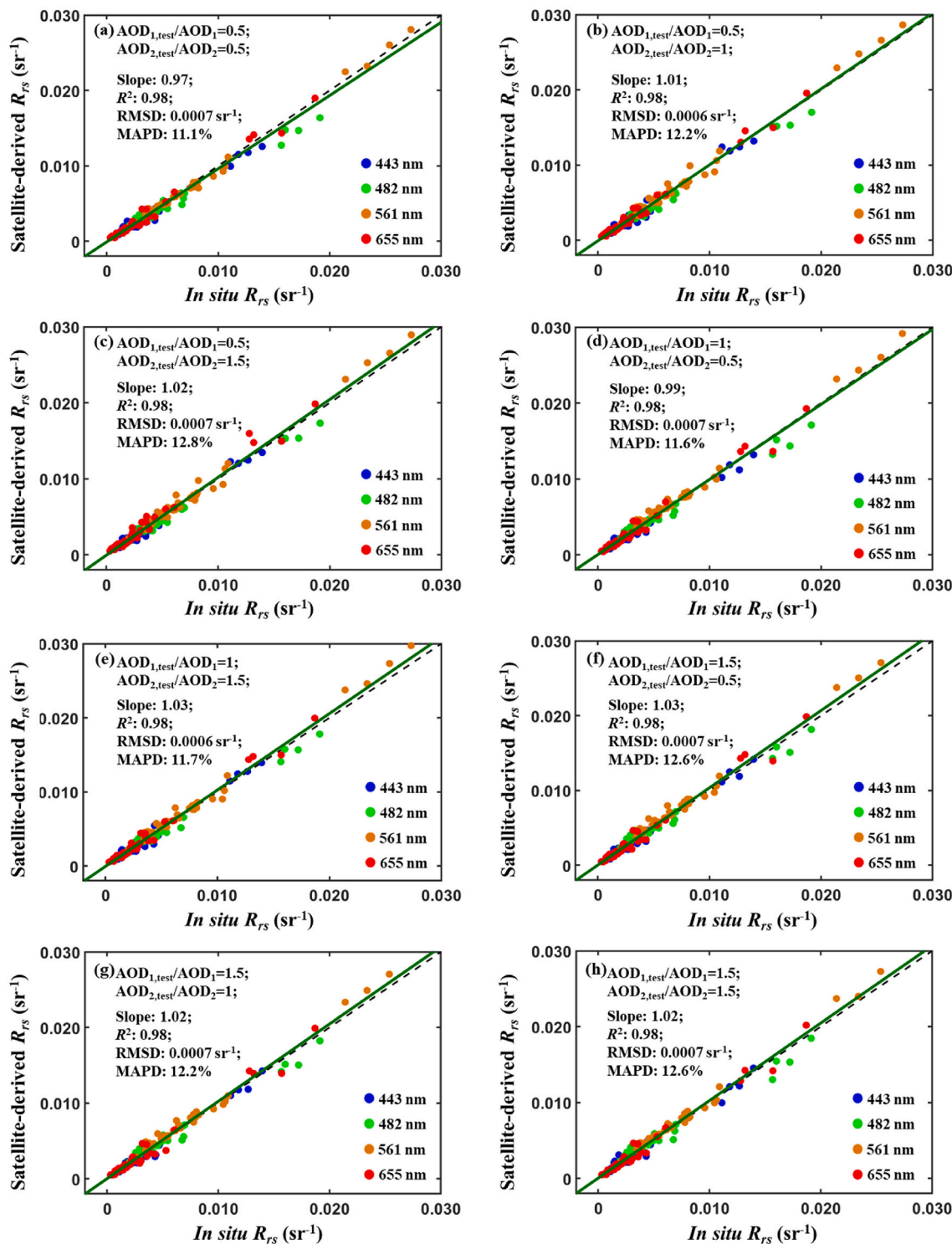


Fig. 14. Overall comparison of R_{rs} at all visible bands (443, 482, 561 and 655 nm) between the retrievals using MPACA and *in situ* measurements after adding $\pm 50\%$ errors to AOD_1 and AOD_2 . The dashed line refers to 1:1 line, and the dark green lines represent the linear regression for all visible bands with the statistical measures shown in the scatterplot. (For interpretation of the references to color in this figure legend, the reader is referred to the web version of this article.)

algorithm (MPACA) based on the assumption that the aerosol type is uniform within a high-spatial-resolution image but allowing water properties to vary freely. The algorithm is evaluated using the Landsat-8 OLI measurements at six different coastal locations, which include turbid waters. It is found that the R_{rs} estimations from MPACA have MAPD of less than 16.2% of *in situ* measurements, which happened at the red band (655 nm), while R_{rs} obtained by SeaDAS and Acolite show

MAPD up to 38.8% and 228.2%, respectively, for the same dataset. These results indicate that MPACA could generate reliable R_{rs} for HSR satellites like Landsat-8 OLI or Sentinel-2 MSI or some small satellites, sensors having two bands in the NIR or SWIR domain, as long as the retrieved AOD(NIR) has an uncertainty less than 50% over turbid coastal waters.

Table 3

Statistics for all matchup sampling stations ($N = 38$) of R_{rs} at all visible bands (443, 482, 561 and 655 nm) between the retrievals using MPACA and *in situ* measurements after adding $\pm 50\%$ errors to AOD_1 and AOD_2 .

R^2		Ratio ($AOD_{1,test}/AOD_1; AOD_{2,test}/AOD_2$)							
		0.5;0.5	0.5;1	0.5;1.5	1;0.5	1;1.5	1.5;0.5	1.5;1	1.5;1.5
(A)									
Band	443	0.98	0.97	0.98	0.98	0.98	0.98	0.98	0.97
	482	0.99	0.99	0.99	0.98	0.99	0.98	0.98	0.98
	561	0.99	0.99	0.99	0.99	0.99	0.99	0.99	0.99
	655	0.98	0.99	0.98	0.98	0.99	0.98	0.98	0.98
(B)									
Band	443	0.0006	0.0005	0.0005	0.0005	0.0004	0.0004	0.0004	0.0005
	482	0.0009	0.0007	0.0006	0.0009	0.0006	0.0007	0.0007	0.0008
	561	0.0005	0.0007	0.0008	0.0006	0.0009	0.0010	0.0009	0.0009
	655	0.0005	0.0005	0.0008	0.0006	0.0006	0.0007	0.0007	0.0006
(C)									
Band	443	12.3	14.7	14.5	13.1	12.6	12.1	10.7	15.2
	482	9.6	9.6	9.2	11.2	9.7	11.7	12.1	12.1
	561	5.0	7.6	8.3	6.9	8.2	9.7	8.6	7.8
	655	16.3	16.8	19.0	15.4	16.4	16.7	17.3	15.2

Declaration of Competing Interest

The authors declare that they have no known competing financial interests or personal relationships that could have appeared to influence the work reported in this paper.

Acknowledgments

Financial support provided by the Chinese Ministry of Science and Technology through the National Key Research and Development Program of China (#2016YFC1400904) and the National Natural Science Foundation of China (#41890803, #41941008, and #41830102), the Joint Polar Satellite System (JPSS) funding for the NOAA ocean color calibration and validation (Cal/Val) project, and the University of Massachusetts Boston is greatly appreciated. The authors would like to thank USGS for the distribution of Landsat-8 OLI L1 imagery, NASA for the SeaDAS processing software, and RBINS for the Acolite processing software. The operators of the AERONET-OC stations worldwide are kindly thanked for their efforts in keeping the stations running and for the use of their data: Brent Holben (COVE_SEAPRISM), Sam Ahmed (LISCO), and Dimitry Van der Zande (Thornton_CPower, Zeebrugge-MOW1). Dr. Pengwang Zhai is also kindly thanked for his helpful suggestions in the preparation and completeness of this paper. We also thank three anonymous reviewers for constructive comments and suggestions that greatly improved this manuscript.

Author contributions

J Wang conducted the study and drafted the manuscript; Z Lee conceptualized the study and finalized the manuscript; D Wang helped processing and analyzing satellite data; S Shang helped data evaluation and finalizing the manuscript; J Wei helped analyzing field measurements and the manuscript; A Gilerson helped analyzing field and AERONET-OC measurements and the manuscript.

Appendix A. Supplementary data

Supplementary data to this article can be found online at <https://doi.org/10.1016/j.rse.2021.112633>.

[org/10.1016/j.rse.2021.112633](https://doi.org/10.1016/j.rse.2021.112633).

References

Ahmad, Z., McClain, C.R., Herman, J.R., Franz, B.A., Kwiatkowska, E.J., Robinson, W.D., Bucsela, E.J., Tzortziou, M., 2007. Atmospheric correction for NO2 absorption in retrieving water-leaving reflectances from the SeaWiFS and MODIS measurements. *Appl. Opt.* 46, 6504–6512.

Ahmad, Z., Franz, B., McClain, C., Kwiatkowska, E., Werdell, J., Shettle, E., Holben, B., 2010. New aerosol models for the retrieval of aerosol optical thickness and normalized water-leaving radiances from the SeaWiFS and MODIS sensors over coastal regions and open oceans. *Appl. Opt.* 49, 5545–5560.

Ahn, J.H., Park, Y.J., Ryu, J.H., Lee, B., Oh, I.S., 2012. Development of atmospheric correction algorithm for Geostationary Ocean Color Imager (GOCI). *Ocean ence J.* 47, 247–259.

Ali, S.M., Gupta, A., Raman, M., Sahay, A., Tirkey, A., 2021. Improved estimates of bio-optical parameters in optically complex water using hyperspectral remote sensing data. *Int. J. Remote Sens.* 42, 3056–3073.

André, J., Morel, A., 1991. Atmospheric corrections and interpretation of marine radiances in CZCS imagery, revisited. *Oceanol. Acta* 14, 3–22.

Bailey, S.W., Werdell, P.J., 2006. A multi-sensor approach for the on-orbit validation of ocean color satellite data products. *Remote Sens. Environ.* 102, 12–23.

Bailey, S.W., Franz, B.A., Werdell, P.J., 2010. Estimation of near-infrared water-leaving reflectance for satellite ocean color data processing. *Opt. Express* 18, 7521–7527.

Ball_BA_RSR.v1.11. <https://landsat.gsfc.nasa.gov/preliminary-spectral-response-of-the-operational-land-imager-in-band-band-average-relative-spectral-response/>.

Bi, S., Li, Y., Wang, Q., Lyu, H., Liu, G., Zheng, Z., Du, C., Mu, M., Xu, J., Lei, S., 2018. Inland water atmospheric correction based on turbidity classification using OLCI and SLSTR synergistic observations. *Remote Sens.* 10, 1002.

Brajard, J., Moulin, C., Thiria, S., 2008. Atmospheric correction of SeaWiFS Ocean color imagery in the presence of absorbing aerosols off the Indian coast using a neuro-variational method. *Geophys. Res. Lett.* 35, 1648–1650.

Brando, V.E., Dekker, A.G., 2003. Satellite hyperspectral remote sensing for estimating estuarine and coastal water quality. *IEEE Trans. Geosci. Remote Sens.* 41, 1378–1387.

Cao, F., Tzortziou, M., Hu, C., Mannino, A., Fichot, C.G., Del Vecchio, R., Najjar, R.G., Novak, M., 2018a. Remote sensing retrievals of colored dissolved organic matter and dissolved organic carbon dynamics in North American estuaries and their margins. *Remote Sens. Environ.* 205, 151–165.

Cao, F., Tzortziou, M., Hu, C., Mannino, A., Fichot, C.G., Vecchio, R.D., Najjar, R.G., Novak, M., 2018b. Remote sensing retrievals of colored dissolved organic matter and dissolved organic carbon dynamics in North American estuaries and their margins. *Remote Sens. Environ.* 205, 151–165.

Chou, M., 1981. Computations of transmittance and radiance in infrared water vapor sounding channels. *Mon. Weather Rev.* 109, 659–665.

Cracknell, A., Newcombe, S., Black, A., Kirby, N., 2001. The ABDMAP (algal bloom detection, monitoring and prediction) concerted action. *Int. J. Remote Sens.* 22, 205–247.

- De Keukelaere, L., Sterckx, S., Adriaensens, S., Knaeps, E., Reusen, I., Giardino, C., Bresciani, M., Hunter, P., Neil, C., Van der Zande, D., 2018. Atmospheric correction of Landsat-8/OLI and Sentinel-2/MSI data using iCOR algorithm: validation for coastal and inland waters. *Eur. J. Remote Sens.* 51, 525–542.
- Dekker, A.G., Phinn, S.R., Anstee, J., Bissett, P., Brandt, V.E., Casey, B., Fearn, P., Hedley, J., Klonowski, W., Lee, Z.-P., Lynch, M., Lyons, M., Mobley, C., Roelfsema, C., 2011. Intercomparison of shallow water bathymetry, hydro-optics, and benthos mapping techniques in Australian and Caribbean coastal environments. *Limnol. Oceanogr. Meth.* 9, 396–425.
- Doerffer, R., Schiller, H., 2007. The MERIS Case 2 water algorithm. *Int. J. Remote Sens.* 28, 517–535.
- Dogliotti, A.I., Ruddick, K., Guerrero, R., 2016. Seasonal and inter-annual turbidity variability in the Río de la Plata from 15 years of MODIS: El Niño dilution effect. *Estuar. Coast. Shelf Sci.* 182, 27–39.
- Doxani, G., Papadopoulou, M., Lafazani, P., Pikridas, C., Tsakiri-Strati, M., 2012. Shallow-water bathymetry over variable bottom types using multispectral Worldview-2 image. *Int. Arch. Photogramm. Rem. Sens. Spat. Inform. Sci.* 39, 159–164.
- Fan, Y., Li, W., Gatebe, C.K., Jamet, C., Zibordi, G., Schroeder, T., Stamnes, K., 2017. Atmospheric correction over coastal waters using multilayer neural networks. *Remote Sens. Environ.* 199, 218–240.
- Fan, Y.Z., Li, W., Chen, N., Ahn, J.H., Park, Y.J., Kratzer, S., Schroeder, T., Ishizaka, J., Chang, R., Stamnes, K., 2020. OC-SMART: a machine learning based data analysis platform for satellite ocean color sensors. *Remote Sens. Environ.* 253, 112236.
- Fettweis, M., Francken, F., Pison, V., Van den Eynde, D., 2006. Suspended particulate matter dynamics and aggregate sizes in a high turbidity area. *Mar. Geol.* 235, 63–74.
- Fettweis, M., Baeye, M., Cardoso, C., Dujardin, A., Lauwaert, B., Van den Eynde, D., Van Hoestenbergh, T., Vanlede, J., Van Poucke, L., Velez, C., 2016. The impact of disposal of fine-grained sediments from maintenance dredging works on SPM concentration and fluid mud in and outside the harbor of Zeebrugge. *Ocean Dyn.* 66, 1497–1516.
- Franz, B.A., Bailey, S.W., Kuring, N., Werdell, P.J., 2015a. Ocean color measurements with the Operational Land Imager on Landsat-8: implementation and evaluation in SeaWiFS. *J. Appl. Remote Sens.* 9, 096070.
- Franz, B.A., Bailey, S.W., Kuring, N., Werdell, P.J., 2015b. Ocean color measurements with the Operational Land Imager on Landsat-8: implementation and evaluation in SeaWiFS. *J. Appl. Rem. Sens.* 9, 1–16.
- Gordon, H.R., 1994. Modeling and simulating radiative transfer in the ocean. In: Spinrad, R.W., Carder, K.L., Perry, M.J. (Eds.), *Ocean Optics*. Oxford University, New York.
- Gordon, H.R., 1997. Atmospheric correction of ocean color imagery in the Earth observing system era. *J. Geophys. Res.* 102, 17081–17106.
- Gordon, H.R., Morel, A., 1983. *Remote Assessment of Ocean Color for Interpretation of Satellite Visible Imagery: A Review*. Springer-Verlag, New York.
- Gordon, H.R., Wang, M., 1992. Surface roughness considerations for atmospheric correction of ocean color sensors. 1: Rayleigh scattering component. *Appl. Opt.* 31, 4247–4260.
- Gordon, H.R., Wang, M., 1994. Retrieval of water-leaving radiance and aerosol optical thickness over oceans with SeaWiFS: a preliminary algorithm. *Appl. Opt.* 33, 443–452.
- Gordon, H.R., Brown, J.W., Evans, R.H., 1988. Exact Rayleigh scattering calculations for use with Nimbus-7 Coastal Zone Color Scanner. *Appl. Opt.* 27, 862–871.
- Harding, W.R., 2015. Living with eutrophication in South Africa: a review of realities and challenges. *Trans. R. Soc. South Afr.* 70, 155–171.
- Hlaing, S., Harmel, T., Ibrahim, A., Ioannou, I., Tonizzo, A., Gilerson, A., Ahmed, S., 2010. Validation of ocean color satellite sensors using coastal observational platform in Long Island Sound. In: *Remote Sensing of the Ocean, Sea Ice, and Large Water Regions 2010*. International Society for Optics and Photonics, p. 782504.
- Hlaing, S., Harmel, T., Gilerson, A., Foster, R., Weidemann, A., Arnone, R., Wang, M., Ahmed, S., 2013. Evaluation of the VIIRS ocean color monitoring performance in coastal regions. *Remote Sens. Environ.* 139, 398–414.
- Holben, B.N., Eck, T.F., Slutsker, I., Tanré, D., Buis, J.P., Setzer, A., Vermote, E., Reagan, J.A., Kaufman, Y.J., Nakajima, T., Lavenu, F., Jankowiak, I., Smirnov, A., 1998. AERONET - a federated instrument network and data archive for aerosol characterization. *Remote Sens. Env.* 66, 1–16.
- Holben, B.N., Tanre, D., Smirnov, A., Eck, T., Slutsker, I., Abuhassan, N., Newcomb, W., Schafer, J., Chatenet, B., Lavenu, F., 2001. An emerging ground-based aerosol climatology: aerosol optical depth from AERONET. *J. Geophys. Res. Atmos.* 106, 12067–12097.
- Hu, C., Carder, K.L., Mueller-Karger, F.E., 2000. Atmospheric correction of SeaWiFS imagery over turbid coastal waters: a practical method. *Remote Sens. Environ.* 74, 195–206.
- Hu, C., Lee, Z., Muller-Karger, F.E., Carder, K.L., Walsh, J.J., 2006. Ocean color reveals phase shift between marine plants and yellow substance. *IEEE Geosci. Remote Sens. Lett.* 3, 262–266.
- Hu, C., Barnes, B.B., Feng, L., Wang, M., Jiang, L., 2019. On the interplay between ocean color data quality and data quantity: impacts of quality control flags. *IEEE Geosci. Remote Sens. Lett.* 17, 745–749.
- Ilori, C.O., Pahlevan, N., Knudby, A., 2019. Analyzing performances of different atmospheric correction techniques for Landsat 8: application for coastal remote sensing. *Remote Sens.* 11, 469.
- IOCCG, 2010. *Atmospheric correction for remotely-sensed ocean-colour products*. In: Wang, M. (Ed.), *Reports of the International Ocean-Colour Coordinating Group*. IOCCG, Dartmouth, Canada, p. 83.
- Kuhn, C., de Matos Valerio, A., Ward, N., Loken, L., Sawakuchi, H.O., Kampel, M., Richey, J., Stadler, P., Crawford, J., Striegl, R., 2019. Performance of Landsat-8 and Sentinel-2 surface reflectance products for river remote sensing retrievals of chlorophyll-a and turbidity. *Remote Sens. Environ.* 224, 104–118.
- Lavender, S.J., Pinkerton, M.H., Moore, G.F., Aiken, J., Blondeau-Patissier, D., 2005. Modification to the atmospheric correction of SeaWiFS ocean colour images over turbid waters. *Cont. Shelf Res.* 25, 539–555.
- Lee, Z., Carder, K.L., Mobley, C.D., Steward, R.G., Patch, J.S., 1999. Hyperspectral remote sensing for shallow waters: 2. Deriving bottom depths and water properties by optimization. *Appl. Opt.* 38, 3831–3843.
- Lee, Z., Casey, B., Arnone, R.A., Weidemann, A.D., Parsons, R., Montes, M.J., Gao, B.-C., Goode, W., Davis, C.O., Dye, J., 2007. Water and bottom properties of a coastal environment derived from Hyperion data measured from the EO-1 spacecraft platform. *J. Appl. Remote Sens.* 1, 011502.
- Lee, Z., Weidemann, A., Arnone, R., 2012. Combined effect of reduced band number and increased bandwidth on shallow water remote sensing: the case of WorldView 2. *IEEE Trans. Geosci. Rem. Sens.* 51 (5), 2577–2586 accepted.
- Lee, Z., Shang, S., Hu, C., Zibordi, G., 2014. Spectral interdependence of remote-sensing reflectance and its implications on the design of ocean color satellite sensors. *Appl. Opt.* 53, 3301–3310.
- Lee, Z.-P., Pahlevan, N., Ahn, Y.-H., Greb, S., O'Donnell, D., 2013. A robust approach to directly measure water-leaving radiance in the field. *Appl. Opt.* 52, 1693–1701.
- Li, J., Hu, C., Shen, Q., Barnes, B.B., Murch, B., Feng, L., Zhang, M., Zhang, B., 2017. Recovering low quality MODIS-Terra data over highly turbid waters through noise reduction and regional vicarious calibration adjustment: a case study in Taihu Lake. *Remote Sens. Environ.* 197, 72–84.
- Lim, J., Choi, M., 2015. Assessment of water quality based on Landsat 8 operational land imager associated with human activities in Korea. *Environ. Monit. Assess.* 187 (384) <https://doi.org/10.1007/s10661-015-4616-1>.
- Ma, J., Yang, S., Wang, X., Qiao, Y., 2006. Atmospheric correction: computing atmospheric diffuse transmittance. *Atmos. Res.* 80, 1–14.
- Majozi, N.P., Salama, M.S., Bernard, S., Harper, D.M., Habte, M.G., 2014. Remote sensing of euphotic depth in shallow tropical inland waters of Lake Naivasha using MERIS data. *Remote Sens. Environ.* 148, 178–189.
- Moore, G.F., Aiken, J., Lavender, S.J., 1999. The atmospheric correction of water colour and the quantitative retrieval of suspended particulate matter in Case II waters: application to MERIS. *Int. J. Remote Sens.* 20, 1713–1733.
- Morel, A., Antoine, D., Gentili, B., 2002. Bidirectional reflectance of oceanic waters: accounting for Raman emission and varying particle scattering phase function. *Appl. Opt.* 41, 6289–6306.
- Pacheco, A., Horta, J., Loureiro, C., Ferreira, Ó., 2015. Retrieval of nearshore bathymetry from Landsat 8 images: a tool for coastal monitoring in shallow waters. *Remote Sens. Environ.* 159, 102–116.
- Pahlevan, N., Lee, Z., Wei, J., Schaaf, C.B., Schott, J.R., Berk, A., 2014. On-orbit radiometric characterization of OLI (Landsat-8) for applications in aquatic remote sensing. *Remote Sens. Environ.* 154, 272–284.
- Pahlevan, N., Roger, J.C., Ahmad, Z., 2017a. Revisiting short-wave-infrared (SWIR) bands for atmospheric correction in coastal waters. *Opt. Express* 25, 6015–6035.
- Pahlevan, N., Schott, J.R., Franz, B.A., Zibordi, G., Markham, B., Bailey, S., Schaaf, C.B., Ondrusek, M., Greb, S., Strait, C.M., 2017b. Landsat 8 remote sensing reflectance (Rrs) products: evaluations, intercomparisons, and enhancements. *Remote Sens. Environ.* 190, 289–301.
- Pahlevan, N., Chittimalli, S.K., Balasubramanian, S.V., Vellucci, V., 2019. Sentinel-2/Landsat-8 product consistency and implications for monitoring aquatic systems. *Remote Sens. Environ.* 220, 19–29.
- Pahlevan, N., Smith, B., Schalles, J., Binding, C.E., Stumpf, R., 2020. Seamless retrievals of chlorophyll-a from Sentinel-2 (MSI) and Sentinel-3 (OLCI) in inland and coastal waters: a machine-learning approach. *Remote Sens. Environ.* 240, 111604.
- Reshitnyk, L., Costa, M., Robinson, C., Dearden, P., 2014. Evaluation of WorldView-2 and acoustic remote sensing for mapping benthic habitats in temperate coastal Pacific waters. *Remote Sens. Environ.* 153, 7–23.
- Steinmetz, F., Deschamps, P.-Y., Ramon, D., 2011. Atmospheric correction in presence of sun glint: application to MERIS. *Opt. Express* 19, 9783–9800.
- Taylor, D.L., 2016. *Boston Harbor Water Quality (1994–2015)*.
- Thuillier, G., Hersé, M., Simon, P., Mandel, H., Gillotay, D., 1998. Observation of the solar spectral irradiance from 200 nm to 870 nm during the ATLAS 1 and ATLAS 2 missions by the SOLSPEC spectrometer. *Metrologia* 35, 689.
- Toming, K., Kutsar, T., Laas, A., Sepp, M., Paaavel, B., Nõges, T., 2016. First experiences in mapping lake water quality parameters with Sentinel-2 MSI imagery. *Remote Sens.* 8, 640.
- Vanhellemont, Q., 2019. Adaptation of the dark spectrum fitting atmospheric correction for aquatic applications of the Landsat and Sentinel-2 archives. *Remote Sens. Environ.* 225, 175–192.
- Vanhellemont, Q., 2020. Sensitivity analysis of the dark spectrum fitting atmospheric correction for metre-and decametre-scale satellite imagery using autonomous hyperspectral radiometry. *Opt. Express* 28, 29948–29965.
- Vanhellemont, Q., Ruddick, K., 2014. Turbid wakes associated with offshore wind turbines observed with Landsat 8, 145, pp. 105–115.
- Vanhellemont, Q., Ruddick, K., 2015. Advantages of high quality SWIR bands for ocean colour processing: examples from Landsat-8. *Remote Sens. Env.* 145, 89–106.
- Vanhellemont, Q., Ruddick, K., 2018. Atmospheric correction of metre-scale optical satellite data for inland and coastal water applications. *Remote Sens. Environ.* 216, 586–597.
- Wang, D., Ronghua, M., Xue, K., Li, J., 2019. Improved atmospheric correction algorithm for Landsat 8-OLI data in turbid waters: a case study for the Lake Taihu, China. *Opt. Express* 27, A1400–A1418.

- Wang, J., Lee, Z., Wei, J., Du, K., 2020. Atmospheric correction in coastal region using same-day observations of different sun-sensor geometries with a revised POLYMER model. *Opt. Express* 28, 26953–26976.
- Wang, M., 1999. Atmospheric correction of ocean color sensors: computing atmospheric diffuse transmittance. *Appl. Opt.* 38, 451–455.
- Wang, M., Bailey, S., 2001. Correction of the sun glint contamination on the SeaWiFS Ocean and atmosphere products. *Appl. Opt.* 40, 4790–4798.
- Wang, M., Shi, W., 2007. The NIR-SWIR combined atmospheric correction approach for MODIS ocean color data processing. *Opt. Express* 15, 15722–15733.
- Wang, M.H., 2002. The Rayleigh lookup tables for the SeaWiFS data processing: accounting for the effects of ocean surface roughness. *Int. J. Remote Sens.* 23, 2693–2702.
- Wang, M.H., 2005. A refinement for the Rayleigh radiance computation with variation of the atmospheric pressure. *Int. J. Remote Sens.* 26, 5651–5663.
- Wei, J., Lee, Z., García, R., Zoffoli, L., Armstrong, R.A., Shang, Z., Sheldon, P., Chen, R.F., 2018. An assessment of Landsat-8 atmospheric correction schemes and remote sensing reflectance products in coral reefs and coastal turbid waters. *Remote Sens. Environ.* 215, 18–32.
- Wei, J., Wang, M., Lee, Z., Briceño, H.O., Yu, X., Jiang, L., García, R., Wang, J., Luis, K., 2020. Shallow water bathymetry with multi-spectral satellite ocean color sensors: leveraging temporal variation in image data. *Remote Sens. Environ.* 250, 112035.
- Werdell, P.J., Franz, B.A., Bailey, S.W., 2010. Evaluation of shortwave infrared atmospheric correction for ocean color remote sensing of Chesapeake Bay. *Remote Sens. Environ.* 114, 2238–2247.
- Xu, Y., Feng, L., Zhao, D., Lu, J., 2020. Assessment of Landsat atmospheric correction methods for water color applications using global AERONET-OC data. *Int. J. Appl. Earth Obs. Geoinf.* 93, 102192.
- Zhu, W., Yu, Q., 2012. Inversion of chromophoric dissolved organic matter from EO-1 Hyperion imagery for turbid estuarine and coastal waters. *IEEE Trans. Geosci. Remote Sens.* 51, 3286–3298.
- Zibordi, G., Holben, B., Slutsker, I., Giles, D., D'Alimonte, D., Melin, F., Berthon, J.-F., Vandemark, D., Feng, H., Schuster, G., Fabbri, B.E., Kaitala, S., Seppala, J., 2009. AERONET-OC: a network for the validation of ocean color primary products. *J. Atmos. Ocean. Technol.* 26, 1634–1651.